Journal of Materials Chemistry B

ROYAL SOCIETY OF CHEMISTRY

PAPER

View Article Online
View Journal | View Issue

Cite this: J. Mater. Chem. B, 2026, 14, 1893

Dual NIR-I excitation and emission-based thermometry and pH-responsive drug delivery using $NaYF_4$:Yb,Er@SiO_2-folic acid conjugates

Sonali Mohanty, [ab] Ian Pompermayer Machado,[a] Jorge García-Balduz, [c] Simona Premcheska, [ac] Andre Skirtach, [c] Kristof Van Hecke [b] and Anna M. Kaczmarek *[a]

Received 18th September 2025,
Accepted 13th January 2026

DOI: 10.1039/d5tb02109j

rsc.li/materials-b

The development of multifunctional host materials capable of simultaneous diagnostics and therapy holds significant promise for biomedical applications. Here, we report the synthesis of $NaYF_4$:Yb,Er particles with cuboidal morphology, designed for optical temperature sensing. To enable controlled drug release, the hydrophobic particles were coated with a mesoporous silica layer to enhance biocompatibility and facilitate dispersion in aqueous solutions and also allowed loading the hybrid material with drug molecules. Surface functionalization with folic acid (FA) further enhanced their potential for targeted delivery applications. Doxorubicin, a chemotherapeutic agent, was successfully loaded into the mesoporous silica shell, allowing for pH-sensitive drug release. Ratiometric upconversion luminescence in both the visible and near-infrared I (NIR-I) region allowed precise temperature monitoring under NIR excitation. The thermometric performance of this system was also evaluated in chicken breast tissue. This work highlights the potential of these hybrid particles as a versatile platform for integrated temperature sensing and drug delivery, with promising applications in theranostics.

Introduction

Luminescence thermometry has emerged as a powerful technique for non-contact and remote temperature sensing across various scientific and biomedical fields. In principle, any luminescent material can serve as a temperature sensor, provided it exhibits thermal, chemical, and optical stability, and demonstrates a measurable dependence of its emission characteristics on temperature.[1,2] Beyond these fundamental requirements, high-performance luminescent thermometric probes must also demonstrate high brightness and high sensitivity. These features are significantly influenced by the characteristics of the host matrix, including its crystalline structure, local symmetry, phonon energy, particle size, and morphology.[3] Among various luminescent materials, inorganic hosts doped with trivalent lanthanide ions (Ln^{3+}) have garnered particular attention due to their exceptional photophysical properties derived from the partially shielded 4f electrons.[4] The unique spectroscopic features of Ln^{3+} enable several thermometric techniques, with lifetime measurements and ratiometric thermometry being the most commonly explored. Among these, ratiometric luminescence thermometry stands out due to its high precision, reliability, self-referenced nature, and lack of dependence on complex instrumentation or frequent calibration.[5,6]

Ratiometric thermometry involves evaluating the ratio of luminescence intensities from two emission bands, which may arise from thermally coupled or non-coupled energy levels. In Boltzmann thermometry, a common approach of ratiometric thermometry, the ratio is derived from thermally coupled levels of a single ion, in which the electronic population follows the Maxwell–Boltzmann distribution. This typically requires an energy gap (ΔE) < 2000 cm^{-1}, as such a gap allows for a measurable population in the excited state at typical operating temperatures, ensuring reliable temperature sensitivity.[7] Aiming at biological applications, a wide range of upconversion nanoparticles (UCNPs) has been explored for ratiometric temperature sensing. Among them, fluoride-based hosts such as $NaYF_4$ have received significant attention due to their low phonon energies (in the range of 300–400 cm^{-1}), which suppress non-radiative losses and enhance luminescence efficiency.[8,9] When co-doped with Yb^{3+} as a sensitizer and Er^{3+} as an activator, $NaYF_4$ exhibits strong upconversion emission, making it one of the most efficient luminescent systems for temperature sensing.[10] Two main

[a] NanoSensing Group, Department of Chemistry, Ghent University, Krijgslaan 281-S3, 9000 Ghent, Belgium. E-mail: Anna.Kaczmarek@UGent.be
[b] XStruct, Department of Chemistry, Ghent University, Krijgslaan 281-S3, 9000 Ghent, Belgium
[c] NanoBioTechnology Group, Department of Biotechnology, Faculty of Bioscience Engineering, Ghent University, 9000 Ghent, Belgium

ratiometric strategies are explored for the Er^{3+},Yb^{3+} UC system, both based on the thermally coupled excited states $^2H_{11/2}$ and $^4S_{3/2}$ of the Er^{3+} ion. The first and most extensively studied strategy corresponds to the Er^{3+} visible emission, more specifically to the $^2H_{11/2} \rightarrow {}^4I_{15/2}$ and $^4S_{3/2} \rightarrow {}^4I_{15/2}$ transitions located in the green region.[5,6,11–13] These are favored due to their strong emission intensity, high signal-to-noise ratio and well-resolved spectral features. The second, less explored but conceptually analogous ratiometric strategy, involves emissions in the near-infrared I (NIR-I) region, wherein it has been reported that the same excited states ($^2H_{11/2}$ and $^4S_{3/2}$) relax to a different lower energy level, $^4I_{13/2}$.[14–16] The small energy gap between $^2H_{11/2}$ and $^4S_{3/2}$ allows their relative population to follow a Boltzmann distribution, providing the foundation for temperature-dependent emission intensity ratios.

The first biological window (NIR-I, 700–1000 nm), has emerged as particularly advantageous optical range for luminescence thermometry, as it allows for deeper tissue penetration and higher spatial resolution with minimal interference from biological autofluorescence.[17] A range of potential thermometric materials has been investigated in the NIR-I region, including organic dyes, quantum dots, semiconductors, and Ln^{3+}-doped nanoparticles.[17–19] Among these, UCNPs are particularly attractive due to their excellent photostability, resistance to photobleaching, long fluorescence lifetimes, and tunable emission spectra. Again, UCNPs offer several benefits for NIR-I optically-driven applications, as they possess high quantum yields, sharp emission peaks, low background interference, and excellent tissue penetration.[5,6,11,20–22] Furthermore, their nanoscale size and surface properties can be engineered for dual-mode applications, such as combining with targeted drug delivery, enabling their use as theranostic agents which integrate diagnostic and therapeutic functions in a single platform.

One of the critical challenges in cancer therapy is the targeted delivery of anticancer drugs to tumor sites while minimizing systemic toxicity. Surface functionalization of nanoparticles with specific biological ligands has emerged as a promising solution. In particular, folic acid (FA) has been widely used due to its ability to bind to folate receptors, which are overexpressed in many cancer cell types, including ovarian, breast, lung, and kidney tumors.[23,24] FA binding triggers receptor-mediated endocytosis, allowing for selective internalization of FA-functionalized nanoparticles into cancer cells.

In this work, we have synthesized $NaYF_4$:Yb,Er particles with a cuboidal morphology, as this shape can promote more efficient cellular uptake due to facet-dependent surface interactions and geometry.[25–27] These as-synthesized $NaYF_4$:Yb,Er particles are initially hydrophobic, as they are prepared in organic solvents and stabilized with oleic acid ligands. To render them suitable for biomedical applications, surface modification was required to convert their hydrophobic surfaces into hydrophilic ones, enabling biocompatibility and dispersibility in aqueous environments. To achieve this, the $NaYF_4$:Yb,Er particles were coated with a mesoporous silica (SiO_2) layer. Compared with other biocompatible or low-immunogenicity coatings, SiO_2 offers several key advantages. It provides excellent hydrophilicity and ensures stable aqueous dispersibility, promoting reliable colloidal behaviour under physiological conditions.[28,29] Silica also forms a chemically inert, optically transparent, and protective non-quenching barrier around the UCNP core, preserving the intrinsic upconversion emission characteristics while offering abundant silanol groups for versatile surface functionalization.[30,31] In contrast, many organic or biologically derived coatings may introduce surface-quenching pathways or undergo structural degradation (such as hydrolysis, oxidation, or desorption) under physiological environments. Additionally, the mesoporous structure allows tunable pore size and high loading capacity for therapeutic or functional molecules, further enhancing its utility in hybrid nanoparticles design.[32,33] These $NaYF_4$:Yb,Er@SiO_2 particles were then functionalized with FA *via* an NHS/DDC-mediated reaction and loaded with the chemotherapeutic agent doxorubicin (DOX), enhancing their potential for targeted drug delivery and cancer therapy. We evaluated the thermometric performance of these particles under NIR-I excitation (975 nm and 940 nm excitation wavelengths) employing ratiometric UC luminescence, in both the visible and NIR-I region. Additionally, we investigated the pH-dependent drug release behavior of DOX from the carriers and demonstrated the temperature sensing capability of the system in a biological tissue environment (chicken breast) under NIR excitation, showing the potential of this platform for biomedical imaging, temperature monitoring, and targeted drug delivery.

Characterization

Transmission electron microscopy (TEM) images were acquired using a JEOL JEM-1010 instrument operating at 100 kV (non-Cs-corrected). Samples were prepared by drop-casting particle suspensions onto 300-mesh, holey carbon-coated copper grids. Powder X-ray diffraction (XRD) patterns were collected with a Rigaku MiniFlex benchtop diffractometer fitted with a rotating sample stage and a D/tex Ultra silicon strip detector, using Cu-Kα radiation (λ = 1.5406 Å) at 40 kV and 15 mA in Bragg–Brentano (θ–2θ) geometry. Zeta potential measurements were performed using a Zetasizer Nano ZS (Malvern Panalytical, Malvern, United Kingdom). Fourier-transform infrared (FTIR) spectroscopy was carried out using a Nicolet iS50R FT-IR spectrometer (Thermo Scientific, USA). UV-visible absorption spectra were recorded on an IMPLEN NanoPhotometer® NP80 (IMPLEN, Germany) on WaveScan mode. Photoluminescence (PL) measurements were performed on an Edinburgh Instruments FLS1000 UV-vis-NIR spectrometer (Edinburgh Instruments, UK), equipped with a double emission monochromator and a R928P photomultiplier tube (Hamamatsu, Japan) as the detection system. Aqueous suspensions were excited by continuous-wave diode lasers at 975 nm (2 W nominal) and 940 nm (1 W nominal); the actual power outputs, measured in DI water with a PM160T-HP power meter (ThorLabs, USA) were 1350 mW (975 nm) and 547 mW (940 nm). Temperature-dependent PL thermometry measurements were achieved by coupling a LUMA 40/E temperature control system (Quantum Northwest, USA) to the FLS1000, collecting data from 20 to 50 °C in 5 °C increments. The samples' temperature was accurately monitored (±0.01 °C) by a Series 500 thermistor

probe (Quantum Northwest, USA) inserted in the cuvette. All spectral data was analyzed using the open-source TeSen software: https://www.tesen.ugent.be.[34]

Cytotoxicity

2D monolayer cell culture

Healthy neonatal Normal Human Dermal Fibroblasts (NHDFs) were purchased from Lonza Bioscience and cultured in FGM-2 Fibroblast Growth Medium-2 BulletKit (Lonza Bioscience) following the manufacturer's protocol. HeLa cells were obtained from ATCC (CCL-2™) and maintained in Dulbecco's Modified Eagle Medium (DMEM, Gibco) supplemented with 10% fetal bovine serum (FBS, Gibco) and 1% penicillin–streptomycin. Both cell lines were grown as monolayers at 37 °C in a humidified atmosphere containing 5% CO_2. At 80–90% confluency, cells were detached with 0.25% trypsin-EDTA (Gibco), followed by and centrifugation at 300×*g* for 5 minutes. Cells were then seeded into 96-well plates at a density of 5000 cells per well. The plates were incubated at 37 °C in a humidified atmosphere containing 5% CO_2 for 24 hours to allow for cell adhesion and stabilization prior to particles treatment.

Cell viability assay

Cytotoxicity assays were performed to assess the effects of DOX-loaded particles $NaYF_4$:Yb,Er@SiO_2-NH_2@FA@DOX on both NHDF and HeLa cervical cancer cell line models. To ensure homogeneous dispersion, nanoparticle powder was initially suspended in the cell growth medium by vortexing for 1 minute, followed by sonication for 10 minutes, prior to adding the suspension to pre-seeded cells. A range of concentrations (0 [control], 1, 2.5, 5, 10, 25, 50, 200 and 500 μg mL^{-1}) were tested in three technical triplicates. Additionally, the particles themselves, $NaYF_4$:Yb,Er@SiO_2-NH_2@FA, without any loaded DOX, were tested on HeLa cells across the same concentration range of 0 to 500 μg mL^{-1}.

Upon addition of the samples, the cell plates were incubated for 24 hours at 37 °C in a 5% CO_2 atmosphere. Subsequently, 20 μL of PrestoBlue HS reagent was added to each well, and the plates were incubated in darkness for another 4 hours at 37 °C and 5% CO_2 following the manufacturer's instructions. The fluorescence emission of the cell plates was measured using a Tecan spectrophotometer equipped with a microplate reader and a 635 nm optical filter. The data were calculated and normalized with respect to the negative controls, adjusted to 100% cell viability using eqn (1):

$$\text{Cell viability [\%]} = \frac{[\text{FI(technical replicate)} - \text{FI(positive controls average)}]}{[\text{FI(negative control)} - \text{FI(positive controls average)}]} \times 100 \quad (1)$$

Drug loading and release studies

To investigate the drug loading and release behavior of $NaYF_4$:Yb,Er@SiO_2-NH_2@FA, we selected doxorubicin hydrochloride (DOX·HCl, referred to as DOX throughout the manuscript) as a model anticancer drug due to its water solubility and clinical relevance (hereafter referred to as DOX). For drug loading, 5 mg of DOX and 5 mg of $NaYF_4$:Yb,Er@SiO_2-NH_2@FA (1 : 1 ratio) were dispersed in 1 mL of PBS pH 7.4 and stirred in the dark at room temperature for 24 h. The particles were then centrifuged (11 000 rpm, 10 min), and the supernatant was analyzed *via* UV-Vis spectroscopy (480 nm) to quantify unbound DOX using a calibration curve (Fig. S12A and B). The drug loading capacity (LC%) and encapsulation efficiency (EE%) were calculated using eqn (2) and (3), respectively.

$$\text{LC\%} = \frac{\text{mass of drug in NaYF}_4\text{:Yb, Er@SiO}_2\text{@FA}}{\text{mass of NaYF}_4\text{:Yb, Er@SiO}_2\text{@FA@DOX}} \times 100 \quad (2)$$

$$\text{EE\%} = \frac{\text{mass of drug in NaYF}_4\text{:Yb, Er@SiO}_2\text{@FA}}{\text{mass of initial DOX}} \times 100 \quad (3)$$

For the release studies, 5 mg of $NaYF_4$:Yb,Er@SiO_2@FA@DOX particles were separately suspended in 0.5 mL of PBS at pH 5.5 and PBS at pH 7.4 to compare the pH-dependent release behavior, and each suspension was placed in a dialysis bag (6–8 kDa cutoff). The bag was immersed in 20 mL of release medium (PBS pH 5.5 or PBS pH 7.4) and incubated at 37 °C with gentle shaking. At predetermined intervals, 3 mL aliquots were withdrawn for UV-Vis analysis (480 nm) and returned to preserve the overall volume and concentration equilibrium. The amount of DOX released was quantified by measuring its absorbance at 480 nm, revealing distinct pH-dependent release kinetics.

Experimental

Materials

Hexadecyltrimethylammonium bromide (CTAB), *N,N′*-dicyclohexylcarbodiimide (DCC), folic acid, *N*-hydroxysuccinimide (NHS), tetraethyl orthosilicate (TEOS, 98%), oleic acid (technical grade, 90%), 1-octadecene (technical grade, 90%) and doxorubicin hydrochloride (DOX·HCl) were purchased from Sigma-Aldrich. Sodium hydroxide (NaOH, ≥99%) was obtained from Carl Roth. Ethanol (96%, analytical reagent grade) was sourced from Chem Lab. 3-Aminopropyl)triethoxysilane (APTES), and dimethyl sulfoxide (DMSO) were purchased from Thermo Fisher Scientific. Lanthanide trifluoroacetate precursors, (CF_3COONa), Y(CF_3COO)$_3$, Yb(CF_3COO)$_3$, and Er(CF_3COO)$_3$, were used as sources of Na^+, Y^{3+}, Yb^{3+}, and Er^{3+} ions, respectively. Deionized (DI) water was used as the solvent unless otherwise specified. Chicken breast was purchased from Delhaize supermarket, Ghent, Belgium. The meat was labelled as ''Kipfilet/Filet de Poulet'' and was cut into slices approximately 2 mm thick and 1 cm in diameter.

Synthesis of $NaYF_4$:18%Yb,2%Er particles

$NaYF_4$:18%Yb,2%Er particles were synthesized using a thermal decomposition method. In the first step CF_3COONa, and Ln(CF_3COO)$_3$ (Ln = Y, Er, Yb) precursors were prepared according to a previously reported protocol.[35] A mixture of 204 mg of sodium trifluoroacetate (CF_3COONa), 342 mg of yttrium trifluoroacetate (Y(CF_3COO)$_3$), 92.2 mg of ytterbium trifluoroacetate (Yb(CF_3COO)$_3$), and 10.12 mg of erbium trifluoroacetate

($Er(CF_3COO)_3$) were dissolved in a solvent mixture consisting of 6 mL of oleic acid and 4 mL of 1-octadecene in a 50 mL three-neck round-bottom flask. The reaction mixture was initially heated to 120 °C under vacuum with constant stirring for 30 minutes to remove water and other volatile impurities. Following this, the system was purged with nitrogen gas, and the temperature was maintained at 120 °C for an additional 30 minutes until a clear yellow solution was obtained. The temperature was then gradually increased to 310 °C under a continuous nitrogen gas flow, and the solution was stirred vigorously for 1.5 hours to facilitate particle formation. Upon completion, the reaction mixture was cooled to room temperature, and the particles were precipitated by the addition of acetone, followed by centrifugation (8000 rpm, 5 min). The precipitate was thoroughly washed 4–5 times with acetone to remove unreacted precursors and excess surface ligands. The resulting product was then dried in an oven at 80 °C for overnight and stored for subsequent silica (SiO_2) coating.

Synthesis of mesoporous silica-coated $NaYF_4$:Yb,Er particles ($NaYF_4$:Yb,Er@SiO_2)

To encapsulate the cuboidal morphology of $NaYF_4$:Yb,Er particles within a mesoporous silica shell, a surfactant-assisted sol–gel method was employed.[36] Initially, 40 mg of hydrophobic $NaYF_4$:Yb,Er particles dispersed in chloroform (1 mL) were added to an aqueous solution (10 mL) containing 360 mg of CTAB. The mixture was sonicated for 30 minutes to facilitate phase transfer, forming a stable colloidal suspension of CTAB-stabilized particles.

The particles were isolated *via* centrifugation (9000 rpm) and redispersed in DI water (1 mL). This washing cycle was repeated three times to remove excess CTAB. The purified particles (1 mL) were then introduced into a dilute CTAB solution (9 mL, 8.2 mg mL^{-1}) containing NaOH (0.1 mL, 0.1 M) to establish a basic environment for silica condensation. The removal of excess CTAB followed by the reintroduction of fresh CTAB was performed intentionally to ensure precise control over the surfactant concentration during the subsequent silica-coating step. And a dilute CTAB solution was required to form micellar templates that guide the uniform condensation of tetraethyl orthosilicate (TEOS) around the $NaYF_4$:Yb,Er nanoparticle cores. This step is essential for producing a well-defined and mesoporous silica shell. After stirring for 30 minutes, 50 μL of TEOS was added dropwise as the silica precursor. The reaction was maintained at 55 °C under continuous stirring overnight to facilitate the formation of a uniform mesoporous silica shell. The resulting $NaYF_4$:Yb,Er@SiO_2 product was collected by centrifugation (6500 rpm) and washed three times with DI and ethanol to remove residual surfactant and unreacted species. The final product was then dried in an oven at 80 °C overnight.

Folic acid conjugation on $NaYF_4$:Yb,Er@SiO_2 particles ($NaYF_4$:Yb,Er@SiO_2-NH_2@FA)

First, 20 mg of $NaYF_4$:Yb,Er@SiO_2 particles were dispersed in 4 mL of ethanol containing 50 μL of APTES and stirred at room temperature for 24 hours to introduce amine functional groups. In parallel, FA (2 mg) was activated by DCC (0.62 mg) and NHS (0.51 mg) in 1 mL of DMSO under dark conditions, also for 24 hours. The activated FA solution was then added to the amine-functionalized particles and stirred overnight at room temperature in the dark.[23,24] After the reaction, the mixture was centrifuged and washed with water and ethanol to obtain the FA-conjugated product, $NaYF_4$:Yb,Er@SiO_2-NH_2@FA.

The full synthesis pathway is illustrated in Scheme 1, showing intermediate steps including amine functionalization ($NaYF_4$:Yb,Er@SiO_2-NH_2). FA was subsequently conjugated *via* an NHS/DDC-mediated reaction to yield $NaYF_4$:Yb,Er@SiO_2-NH_2@FA.

Results and discussion

$NaYF_4$:Yb,Er@SiO_2-NH_2@FA characterization

TEM images of $NaYF_4$:Yb,Er particles show a prominent cuboidal morphology with an average particle size of approximately 204 nm. While a mixture of hexagonal and cuboidal particles is observed, the cuboidal form is clearly dominant in the sample (Fig. 1A). Following SiO_2 coating, the particles retain this morphology (Fig. 1B), with a SiO_2 shell thickness of approximately 35 nm, as confirmed by the TEM images and size distribution histograms (Fig. S1A and B). Fig. 1C presents the $NaYF_4$:Yb,Er@SiO_2-NH_2@FA particles after FA conjugation, with no observable changes in particle morphology, indicating that the overall structure is

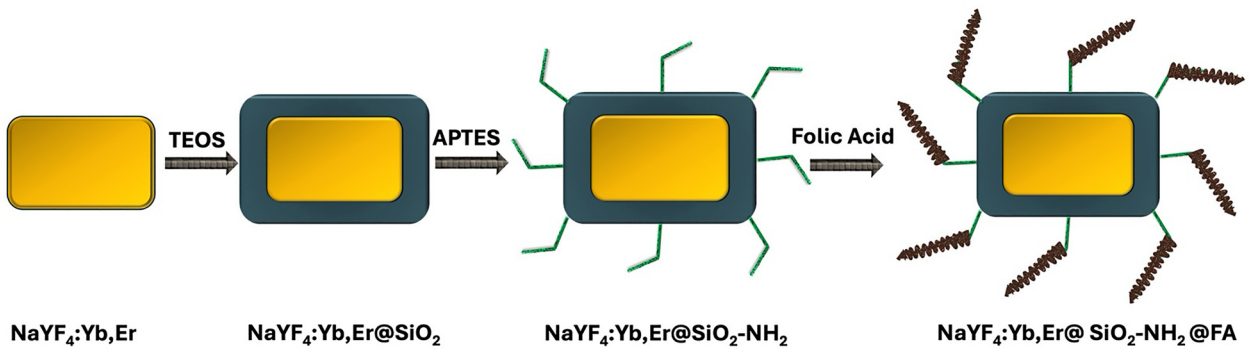

Scheme 1 Stepwise synthesis of FA-conjugated particles: $NaYF_4$:Yb,Er core particles, coating of $NaYF_4$ particles with a silica shell ($NaYF_4$:Yb,Er@SiO_2), amine functionalization using APTES to form $NaYF_4$:Yb,Er@SiO_2-NH_2 and conjugation of FA to the amine-functionalized surface, forming $NaYF_4$:Yb,Er@SiO_2-NH_2@FA.

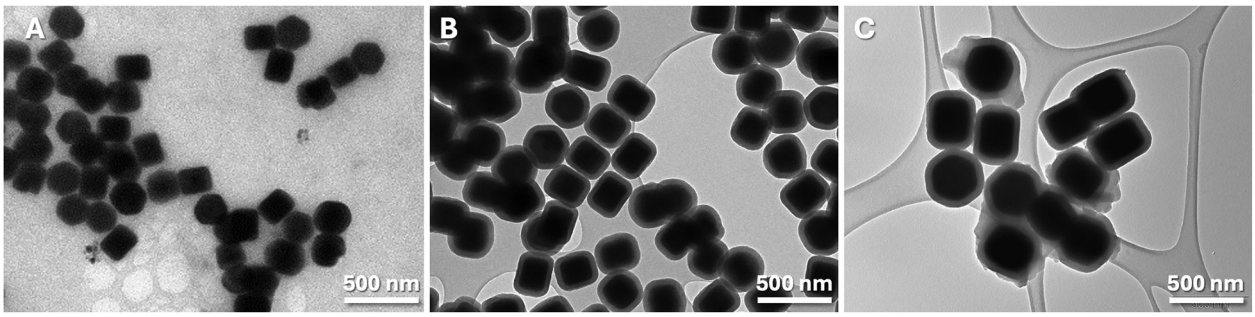

Fig. 1 TEM images of (A) $NaYF_4$:Yb,Er[a], (B) $NaYF_4$:Yb,Er@SiO_2 and (C) $NaYF_4$:Yb,Er@SiO_2-NH_2@FA. [a]Resolution in Fig. 1A is slightly compromised due to the presence of excess OA ligands in the sample.

preserved after FA attachment. The FA-conjugated particles exhibit an average size of approximately 400 nm along their long axis and 300 nm along their short axis, consistent with the dimensions observed in the TEM analysis.

UV-Vis and FTIR analyses played a critical role in confirming both the successful SiO_2 coating on $NaYF_4$:Yb,Er and the subsequent conjugation of FA. UV-Vis spectroscopy showed no characteristic absorption bands for $NaYF_4$:Yb,Er@SiO_2, as is expected considering the absence of any chromophores at this stage of the material preparation. In contrast, $NaYF_4$:Yb,Er@SiO_2-NH_2@FA exhibited distinct absorption bands around 288 nm and 360 nm, corresponding to the π–π* and n–π* transitions of the FA moieties, suggesting effective functionalization of the mesoporous SiO_2 shell with FA (Fig. 2A). Subsequently, FTIR analysis was performed to further validate the functionalization of FA on the $NaYF_4$:Yb,Er@SiO_2-NH_2 particles. The absorption bands observed in the 1600–1450 cm^{-1} region of the FTIR spectrum of the as-synthesized $NaYF_4$:Yb,Er particles correspond to the asymmetric and symmetric stretching vibrations of the carboxylate (COO^-) groups of the oleic-acid ligands bound to the UCNP surface. In the FTIR spectra of both $NaYF_4$:Yb,Er@SiO_2 and $NaYF_4$:Yb,Er@SiO_2-NH_2@FA, a prominent peak observed around 1100 cm^{-1} is assigned to the asymmetric stretching vibrations of Si–O–Si, confirming the presence of the silica shell (Fig. 2B). As shown in Fig. 2B, the $NaYF_4$:Yb,Er@SiO_2 sample displays only the characteristic Si–O–Si stretching band at ~1100 cm^{-1} and no C–H stretching peaks at 2850–2950 cm^{-1} or CH_2 bending near 1470 cm^{-1}, which would indicate the presence of CTAB. This confirms that the surfactant was completely removed during purification, and the particles used in subsequent experiments were CTAB-free. Additionally, in the spectrum of $NaYF_4$:Yb,Er@SiO_2-NH_2@FA, three new peaks appear at approximately 1450 cm^{-1}, 1550 cm^{-1}, and

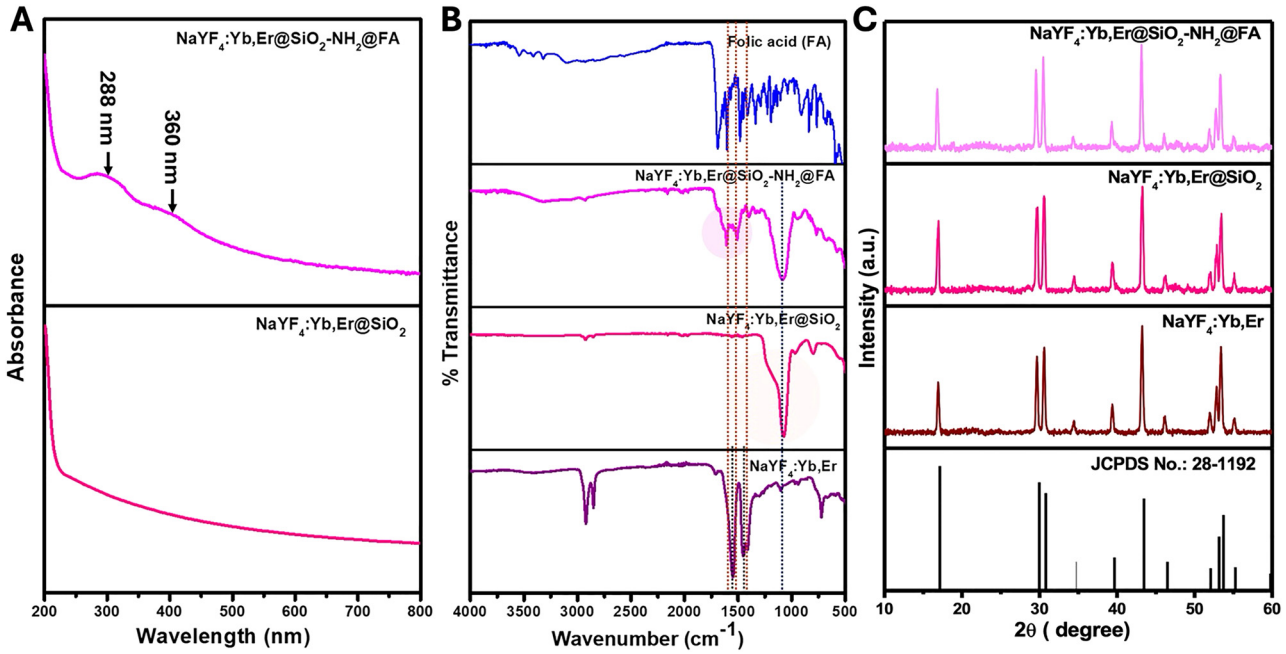

Fig. 2 (A) UV-Vis spectra of $NaYF_4$:Yb,Er@SiO_2 and $NaYF_4$:Yb,Er@SiO_2-NH_2@FA, (B) FTIR spectra, and (C) XRD patterns of $NaYF_4$:Yb,Er, $NaYF_4$:Yb,Er@SiO_2 and $NaYF_4$:Yb,Er@SiO_2-NH_2@FA. (B) also includes the FTIR spectrum of folic acid (FA) registered for band-assignment purposes, while (C) exhibits the reference XRD pattern for the β-$NaYF_4$ structure (JCPDS 28-1192).

1650 cm^{-1}, corresponding to C–N stretching, N–H bending, and C═O stretching vibrations, respectively, which are characteristic of FA functional groups. These peaks further indicate the successful conjugation of FA onto the silica-coated particles. XRD analysis was performed to confirm the crystallographic structure and the phase purity of the synthesized particles. The diffraction peaks of all samples match well with the standard JCPDS reference pattern (JCPDS No. 28-1192), confirming the formation of a pure hexagonal phase structure. This phase crystallizes in a hexagonal close-packed lattice with space group $P6_3/m$, in which Y^{3+} ions, partially substituted by Yb^{3+} and Er^{3+} dopants, occupy cationic sites coordinated by F^- anions.[37,38] The β-phase structure provides lower lattice symmetry and distinct crystal-field environments around the lanthanide ions, which is advantageous for efficient upconversion luminescence as the β-phase structure is known to offer greater luminescent efficiency compared to the cubic phase, owing to reduced nonradiative relaxation pathways.[39–41] No significant changes were observed in the diffraction patterns after SiO_2 coating and subsequent FA conjugation, indicating that the crystalline phase of the core particles remained intact throughout the surface modification processes (Fig. 2C). Zeta potential measurements were performed to assess the colloidal stability and surface charge changes during the surface modification of the particles. The $NaYF_4$:Yb,Er@SiO_2 particles exhibited a high positive zeta potential of +39.3 mV (Fig. S2A), which is most likely attributed to the presence of residual CTAB adsorbed on the silica surface following the coating process.[42] This strong positive surface charge promotes electrostatic repulsion between particles, thereby enhancing colloidal stability in aqueous suspension. During FA conjugation, amine groups were introduced to the $NaYF_4$:Yb,Er@SiO_2-NH_2@FA surface using APTES, enabling covalent attachment of FA *via* its carboxyl groups through the formation of amide bonds. Following conjugation, the zeta potential decreased to +13.2 mV (Fig. S2B), indicating successful surface modification. This reduction is consistent with the introduction of FA's negatively charged carboxyl groups, which partially neutralize the positively charged amine groups on the surface. Despite the decrease, the particles remained colloidally stable in water, likely due to a combination of electrostatic and steric stabilization provided by the FA moieties. In general, particles with a positive surface charge exhibit higher cellular uptake efficiency due to their enhanced interaction with the negatively charged cell membrane.[27] It is worth noting that the bare $NaYF_4$:Yb,Er particles (prior to SiO_2 coating) were not dispersible in water due to the hydrophobic oleic acid surface, and therefore a reliable zeta potential measurement could not be obtained under these conditions. The silica coating was essential to render the particles hydrophilic and suitable for biological applications.

Temperature-dependent luminescence studies in water

Er^{3+} doped into suitable host lattices exhibit rich photoluminescence behavior due to their ladder-like 4f energy level structure (Scheme 2). These emissions, especially in the visible and NIR regions, originate from transitions between thermally populated multiplet levels, making Er^{3+} ions, particularly suitable for ratiometric-based optical thermometry. Among these, the thermally coupled excited states $^2H_{11/2}$ and $^4S_{3/2}$ are of particular interest due to their small energy gap of approximately 700 cm^{-1}, which allows for efficient thermal population redistribution in accordance with the Boltzmann law. When

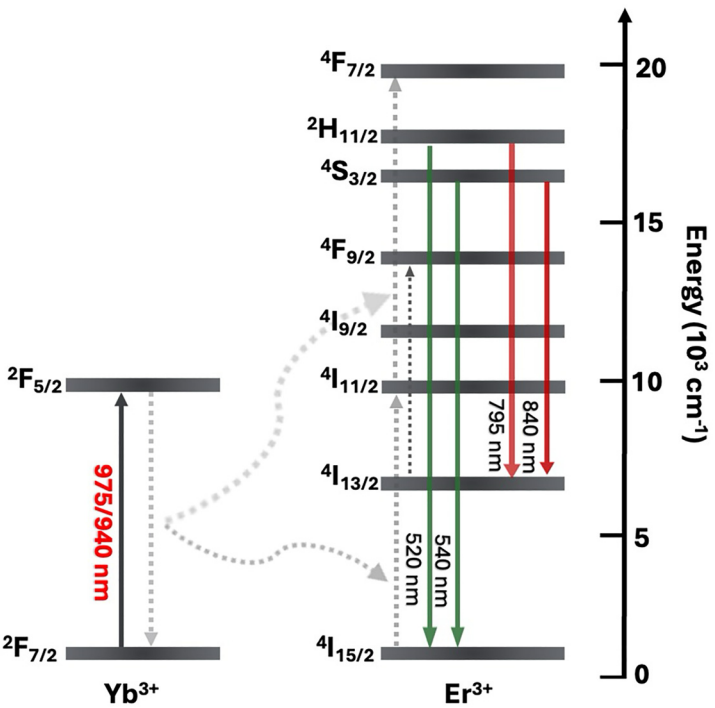

Scheme 2 Energy diagram for Yb^{3+}–Er^{3+} system, excited at 975 nm or 940 nm highlight the excitation mechanisms, emission bands, and electronic transitions relevant to luminescence thermometry.

Er^{3+} is excited (*via* 975 nm or 940 nm excitation, sensitized by Yb^{3+}), electrons are promoted to higher-lying energy levels such as $^4F_{7/2}$, then relax non-radiatively to populate the $^2H_{11/2}$ and $^4S_{3/2}$ states. These two levels can relax radiatively through the $^2H_{11/2} \rightarrow {}^4I_{15/2}$ and $^4S_{3/2} \rightarrow {}^4I_{15/2}$ transitions, resulting in visible-range emissions at approximately 520 nm and 540 nm, respectively. Simultaneously, emissions from these same thermally coupled levels to the $^4I_{13/2}$ ground state give rise to NIR bands centered around 795 nm ($^2H_{11/2} \rightarrow {}^4I_{13/2}$) and 840 nm ($^4S_{3/2} \rightarrow {}^4I_{13/2}$).[14,15,35] These emissions are typically weaker and more host-sensitive than the green emissions but could offer significant advantages in a biological and optoelectronic contexts due to reduced scattering and deeper tissue penetration. The relative populations of $^2H_{11/2}$ and $^4S_{3/2}$ levels vary as a function of temperature, thereby altering the intensity ratios of both the green (520/540 nm) and NIR (795/840 nm) emissions, allowing for precise and non-contact ratiometric temperature readouts. Moreover, we systematically studied the thermometric performance of these two ratiometric approaches by evaluating their relative sensitivities under excitation at 975 nm and 940 nm over a temperature range of 293–323 K.

In the Yb–Er UC system, the standard excitation wavelength is typically around 975 or 980 nm, as this wavelength corresponds closely to the maximum absorption peak of Yb^{3+} ions. This optimal excitation facilitates efficient energy transfer to the Er^{3+} ions, which then emit visible light in the green and red regions. The strong absorption of Yb^{3+} at this wavelength ensures high upconversion efficiency, making 975/980 nm the go-to choice for many applications. However, the use of 975 nm excitation also presents a significant limitation when applied to biological systems. One of the primary issues is that water exhibits a pronounced absorption band around 975 nm, leading to substantial heating effects.[43] In biological environments, this heat generation can cause damage to tissues or interfere with precise measurements in imaging and sensing applications, where thermal effects must be minimized. In contrast, 940 nm excitation offers a promising alternative. Although it does not coincide with the peak of the Yb^{3+} absorption band, it still provides reasonable excitation efficiency for the Yb-Er system. The key advantage of using 940 nm is that it significantly reduces water absorption, thus minimizing the risk of heating in biological systems. This makes 940 nm an alternative choice for biological imaging and sensing, where controlling temperature and avoiding tissue damage are critical considerations.

Although both 975 nm and 940 nm excitation were studied, 975 nm was used as the primary excitation source for all comparisons among $NaYF_4$:Yb,Er, $NaYF_4$:Yb,Er@SiO_2, $NaYF_4$:Yb,Er@SiO_2-NH_2@FA, and $NaYF_4$:Yb,Er@SiO_2-NH_2@FA@DOX to ensure consistent excitation conditions. The available 975 nm laser offered higher power output and more efficient upconversion, enabling strong NIR-I emission even in DOX-loaded samples and through biological tissue. In contrast, a high-power 940 nm excitation source was not available, and the lower power of the 940 nm laser limited its performance under similar conditions. Therefore, 940 nm data were included as a supplementary demonstration of alternative excitation feasibility but not intended for direct power-matched comparison. Importantly, our aim was to demonstrate bio-application feasibility using the best available excitation conditions, and under these conditions, 975 nm excitation consistently provided strong NIR-I emission, making it the primary excitation source used in this study.

To characterize the thermometric performance of the $NaYF_4$:Yb,Er-based systems, the emission intensity ratio (Δ) was calculated between two Er^{3+} transitions: (i) 520 nm ($^2H_{11/2} \rightarrow {}^4I_{15/2}$) and 540 nm ($^4S_{3/2} \rightarrow {}^4I_{15/2}$), or (ii) 795 nm ($^2H_{11/2} \rightarrow {}^4I_{13/2}$) and 840 nm ($^4S_{3/2} \rightarrow {}^4I_{13/2}$). This ratio is defined through eqn (4):

$$\Delta = \frac{I_1}{I_2} \tag{4}$$

Here I_1 and I_2 represent the integrated intensities at the respective wavelengths.

According to the Boltzmann distribution, Δ follows an exponential dependence on temperature (eqn (5)):

$$\Delta = \alpha \exp\left(-\frac{\Delta E}{k_B T}\right) \tag{5}$$

where $\alpha = C \times (g_2/g_1)$, accounting for the degeneracy ratio (g_2/g_1) and relative transition probabilities (C). ΔE is the energy difference between the two excited states, k_B is the Boltzmann constant, and T is the absolute temperature (K).

To quantitatively compare the thermal sensitivity of different luminescent thermometers, the relative sensitivity (S_r) is defined as the rate of change of the intensity ratio with respect to temperature (eqn (6)):

$$S_r = 100\% \times \left|\frac{1}{\Delta}\frac{\partial \Delta}{\partial T}\right| \tag{6}$$

Finally, the temperature uncertainty (σT), a key parameter indicating the precision of temperature determination, as it considers both the relative sensitivity and the measurement error of the intensity ratio ($\delta\Delta$; eqn (7)).[44,45]

$$\sigma T = \frac{1}{S_r}\sqrt{\frac{1}{I_1} + \frac{1}{I_2}} \tag{7}$$

To evaluate the thermometric performance, we investigated $NaYF_4$:Yb,Er dispersed in cyclohexane, and SiO_2-coated $NaYF_4$:Yb,Er ($NaYF_4$:Yb,Er@SiO_2) and folic acid-conjugated $NaYF_4$:Yb,Er@SiO_2 ($NaYF_4$:Yb,Er@SiO_2-NH_2@FA), both dispersed in water at a concentration of 3 mg mL^{-1}. All samples were excited using a 975 nm laser (1350 mW), and their emissions were first studied in the visible region. To evaluate temperature sensitivity, the intensity ratio of the thermally coupled levels, which emit at approximately 520 nm and 540 nm, was used to define the thermometric parameter Δ (as described by eqn (4)), which follows a Boltzmann-type dependence. The experimental data were fitted using the model described in eqn (5), and from this fit, the ΔE between the two levels was obtained. The obtained ΔE value is in good agreement with reported values for similar Yb–Er systems.[5,6,11,46] For $NaYF_4$:Yb,Er in cyclohexane (Fig. S3A–D), ΔE was found to be 741 cm^{-1} with a correlation

coefficient (R^2) of 0.998. After coating with SiO_2 ($NaYF_4$:Yb,Er@SiO_2) (Fig. 3A–D), the ΔE was 767 cm^{-1} (R^2 = 0.998), while after conjugation with folic acid (Fig. 4A–D), ΔE was calculated to be 716 cm^{-1} (R^2 = 0.999). The S_r, calculated using eqn (6), was 1.242% K^{-1} for the uncoated sample, 1.285% K^{-1} after SiO_2 coating, and 1.201% K^{-1} for the FA-conjugated material ($NaYF_4$:Yb,Er@SiO_2-NH_2@FA). Corresponding σT, calculated using eqn (7), were approximately 0.16 K, 0.15 K, and 0.15 K, respectively. A summary of these findings is presented in Table 1. No significant change in relative sensitivity was observed after SiO_2 coating or folic acid conjugation, indicating that the local chemical environment has a minimal influence on the luminescent thermometric properties. This highlights the stability and reliability of the system for optical thermometry applications.

In addition to the visible range, we also investigated thermometric behavior of the bands in the NIR-I region at 795 nm ($^4H_{11/2} \rightarrow {}^4I_{13/2}$) and 840 nm ($^4S_{3/2} \rightarrow {}^4I_{13/2}$), which also originate from thermally coupled levels. For $NaYF_4$:Yb,Er in cyclohexane, ΔE was calculated to be 563 cm^{-1} with R^2 = 0.999, and the relative sensitivity was 0.944% K^{-1} with a temperature uncertainty of 0.29 K (Fig. S4A–D). The SiO_2-coated material ($NaYF_4$:Yb,Er@SiO_2) showed a ΔE of 601 cm^{-1} (R^2 = 0.975), S_r of 1.008% K^{-1}, and σT of 0.39 K (Fig. 5A–D), while the FA-conjugated version exhibited a ΔE of 593 cm^{-1} (R^2 = 0.989), S_r of 0.995% K^{-1}, and σT of 0.22 K (Fig. 6A–D). These results are summarized in Table 2. The energy gap between the $^2H_{11/2}$ and $^4S_{3/2}$ levels is consistent with theoretical expectations, supporting the reliability of these transitions for temperature sensing in the NIR-I region.[6,16] Once again, no significant variation in relative sensitivity was detected across the different surface modifications, supporting the conclusion that the system maintains high thermal sensitivity regardless of its surrounding matrix.

To further investigate the thermometric performance of the samples, measurements were also carried out using 940 nm laser excitation. As mentioned earlier, this excitation wavelength is known to induce less heating than 975 nm, which can be advantageous for sensitive biological or temperature-critical applications. The samples were dispersed in water at a concentration of 3 mg mL^{-1}, similar to the previous experiments. The samples $NaYF_4$:Yb,Er (Fig. S5A–D), $NaYF_4$:Yb,Er@SiO_2 (Fig. 7A–D) and $NaYF_4$:Yb,Er@SiO_2-NH_2@FA (Fig. 8A–D) were first evaluated in the visible range within the physiological temperature range of 20–50 °C, and the results are summarized in Table 3. Thermometric performance was assessed by analyzing the intensity ratio of emissions from the thermally coupled $^2H_{11/2}$ and $^4S_{3/2}$ levels of Er^{3+}. These results indicate that the relative sensitivity of the samples under 940 nm excitation is comparable to that under 975 nm excitation, suggesting that 940 nm excitation still provides reliable and effective thermometric performance. This further demonstrates the potential of these materials as efficient temperature sensors, even with lower heating effects.

Furthermore, we extended our study to the NIR-I spectral region under the same 940 nm excitation conditions for $NaYF_4$:Yb,Er (Fig. S6A–D), $NaYF_4$:Yb,Er@SiO_2 (Fig. 9A–D) and $NaYF_4$:Yb,Er@SiO_2-NH_2@FA (Fig. 10A–D), evaluating the emission bands corresponding to the $^2H_{11/2} \rightarrow {}^4I_{13/2}$ and $^4S_{3/2} \rightarrow {}^4I_{13/2}$

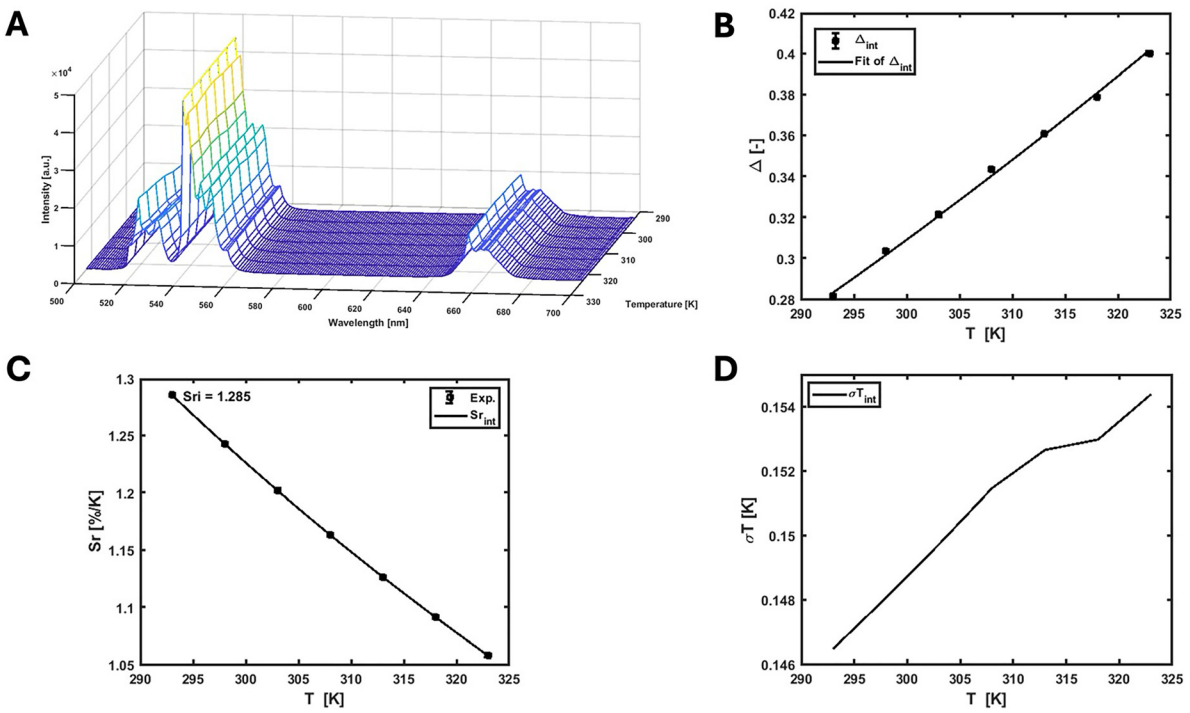

Fig. 3 (A) Emission map of $NaYF_4$:Yb,Er@SiO_2 dispersed in water was recorded across the temperature range of 293.15–323.15 K (20–50 °C) in the visible region ($^2H_{11/2} \rightarrow {}^4I_{15/2}$ and $^4S_{3/2} \rightarrow {}^4I_{15/2}$) under 975 nm excitation, (B) graph showing the Δ parameter *versus* temperature. The points show the experimental Δ values, and the solid line shows the least squares fit to the experimental points. (C) Plot of the relative sensitivity (S_r) at varying temperatures. (D) Plot of the temperature uncertainty (σT) at varying temperatures.

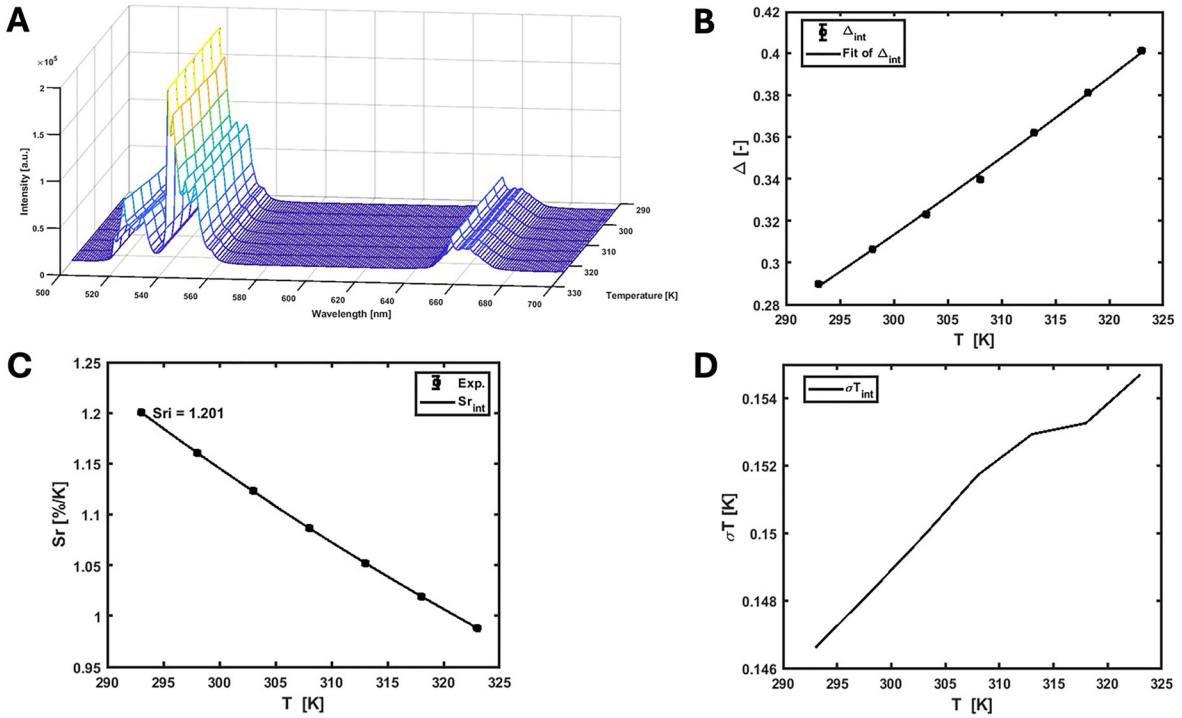

Fig. 4 (A) Emission map of $NaYF_4$:Yb,Er@SiO_2-NH_2@FA dispersed in water, recorded across the temperature range of 293.15–323.15 K (20–50 °C) in the visible region ($^2H_{11/2} \rightarrow {}^4I_{15/2}$ and $^4S_{3/2} \rightarrow {}^4I_{15/2}$) under 975 nm excitation, (B) graph showing the Δ parameter *versus* temperature. The points show the experimental Δ values, and the solid line shows the least squares fit to the experimental points. (C) Plot of the relative sensitivity (S_r) at varying temperatures. (D) Plot of the temperature uncertainty (σT) at varying temperatures.

Table 1 Thermometric parameters in the visible range under 975 nm excitation, performed in water unless otherwise specified

Compounds	R^2	ΔE (cm^{-1})	S_r (% K^{-1})	σT (K)
$NaYF_4$:18%Yb,2%Er (cyclohexane)	0.998	741	1.242	0.16
$NaYF_4$:18%Yb,2%Er@SiO_2	0.998	767	1.285	0.15
$NaYF_4$:18%Yb,2%Er@SiO_2–NH_2@FA	0.999	716	1.201	0.15
$NaYF_4$:18%Yb,2%Er@SiO_2–NH_2@FA@DOX	0.988	564	0.946	0.67

transitions for temperature sensing. The results, summarized in Table 4, indicate a significant enhancement in relative sensitivity for the $NaYF_4$:Yb,Er@SiO_2 and $NaYF_4$:Yb,Er@SiO_2-NH_2@FA in the NIR-I region at 940 nm compared to 975 nm excitation. This increased sensitivity can be attributed to three main factors: (1) the reduced photothermal effect at 940 nm, which facilitates a more accurate thermal population distribution between the coupled energy levels, leading to a more precise thermometric response,[47,48] (2) lower water absorption at 940 nm, allowing deeper penetration in the cuvette and more efficient excitation of the particles; and (3) enhanced slit sizes, which caused some changes to the peak shape and affected the emission intensity ratios. These findings highlight the effectiveness of $NaYF_4$-based systems as reliable optical thermometers across two different excitation conditions.

Given the promising thermometric performance of the $NaYF_4$:Yb,Er@SiO_2 system observed in the NIR-I region under 940 nm excitation, we further extended our investigation to evaluate its behavior over a wider temperature range (20–80 °C). The particles exhibited an energy gap (ΔE) of 867 cm^{-1} (R^2 = 0.960) and achieved a S_r of 1.454% K^{-1}, with σT of less than 0.90 K (Fig. S7A–D). These results highlight the effectiveness of $NaYF_4$:Yb,Er@SiO_2 as a luminescent thermometer in the NIR-I region, particularly in high-temperature regimes and under low-heating excitation conditions, where both sensitivity and resolution are critical for accurate thermal monitoring. A comprehensive comparison of luminescent thermometers operating in the NIR-I region is presented in Table 5.

To assess whether the material can reliably function as a thermometer for repeated use, cycle tests must be performed. The repeatability is then quantified using eqn (8):

$$R = 1 - \frac{\max|\Delta_c - \Delta_i|}{\Delta_c} \quad (8)$$

Here, Δ_c represents the average value of the thermometric parameter, while Δ_i refers to the individual measurement values of that parameter. This equation helps quantify the consistency of the measurements across multiple cycles, providing insight into the material's reliability over time.

Cycle tests of $NaYF_4$:Yb,Er@SiO_2-NH_2@FA in DI water were performed in the NIR-I range with excitations at 975 nm and 940 nm, spanning repeated heating–cooling cycles between 293.15 K and 323.15 K, to evaluate its potential as a reliable thermometer for physiological temperature ranges (Fig. S8A and B). The results demonstrated that the material exhibited

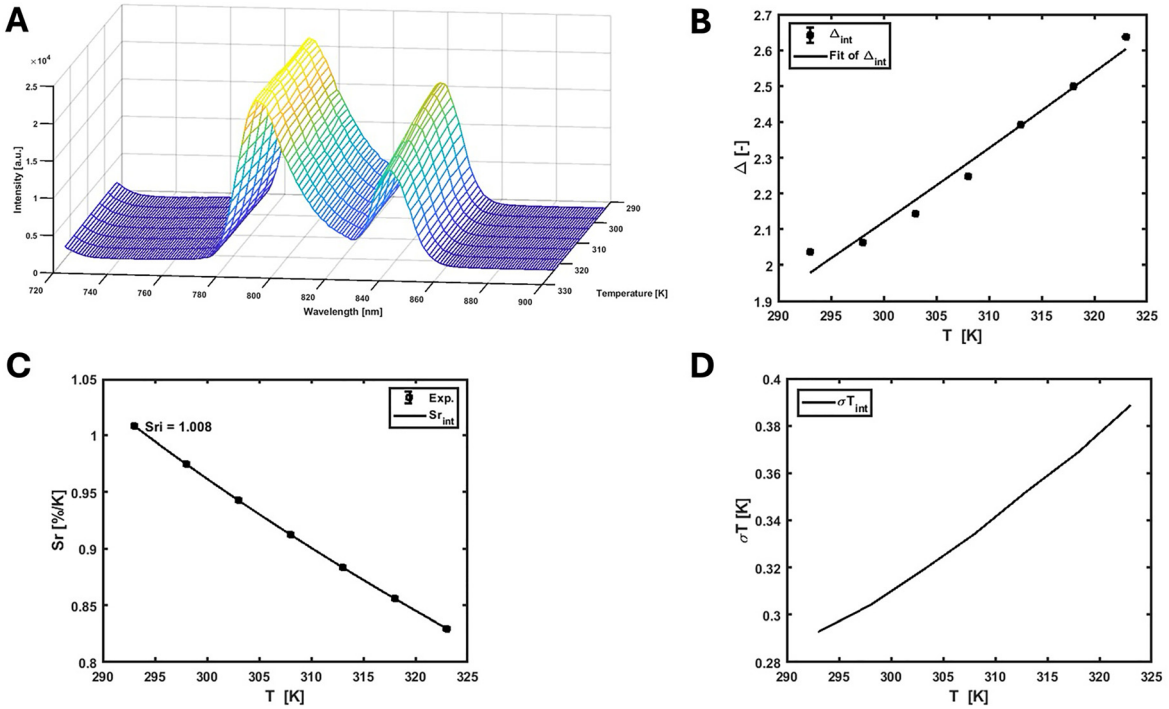

Fig. 5 (A) Emission map of NaYF4:Yb,Er@SiO_2 dispersed in water, recorded across the temperature range of 293.15–323.15 K (20–50 °C) in the NIR-I region ($^2H_{11/2} \rightarrow {}^4I_{13/2}$ and $^4S_{3/2} \rightarrow {}^4I_{13/2}$) under 975 nm excitation, (B) graph showing the Δ parameter *versus* temperature. The points show the experimental Δ values, and the solid line shows the least squares fit to the experimental points. (C) Plot of the relative sensitivity (S_r) at varying temperatures. (D) Plot of the temperature uncertainty (σT) at varying temperatures.

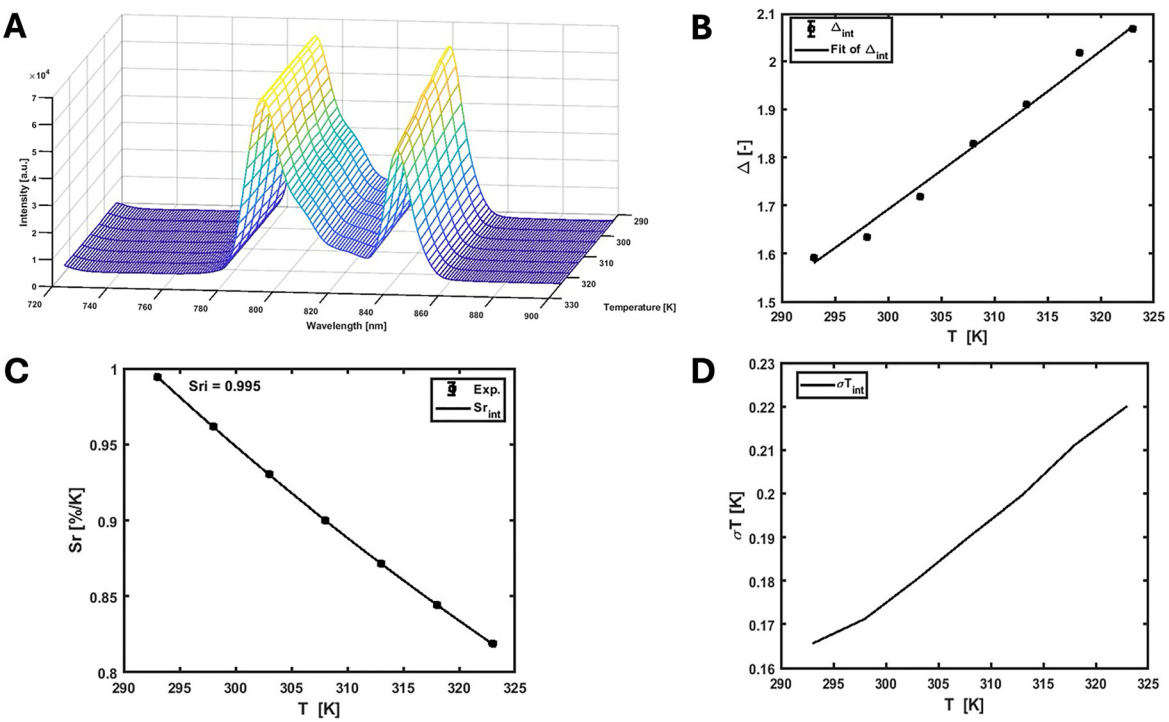

Fig. 6 (A) Emission map of $NaYF_4$:Yb,Er@SiO_2-NH_2@FA dispersed in water, recorded across the temperature range of 293.15–323.15 K (20–50 °C) in the NIR-I region ($^2H_{11/2} \rightarrow {}^4I_{13/2}$ and $^4S_{3/2} \rightarrow {}^4I_{13/2}$) under 975 nm excitation, (B) graph showing the Δ parameter *versus* temperature. The points show the experimental Δ values, and the solid line shows the least squares fit to the experimental points. (C) Plot of the relative sensitivity (S_r) at varying temperatures. (D) Plot of the temperature uncertainty (σT) at varying temperatures.

Table 2 Thermometric parameters in the NIR-I range under 975 nm excitation, performed in water unless otherwise specified

Compounds	R^2	ΔE (cm^{-1})	S_r (% K^{-1})	σT (K)
$NaYF_4$:18%Yb,2%Er (cyclohexane)	0.999	563	0.944	0.29
$NaYF_4$:18%Yb,2%Er@SiO_2	0.975	601	1.008	0.39
$NaYF_4$:18%Yb,2%Er@SiO_2–NH_2@FA	0.989	593	0.995	0.22
$NaYF_4$:18%Yb,2%Er@SiO_2–NH_2@FA@DOX	0.988	607	1.018	0.25
$NaYF_4$:18%Yb,2%Er@SiO_2–NH_2@FA (through chicken breast tissue)	0.988	679	1.138	0.52
$NaYF_4$:18%Yb,2%Er@SiO_2–NH_2@FA@DOX (through chicken breast tissue)	0.993	545	0.913	0.75

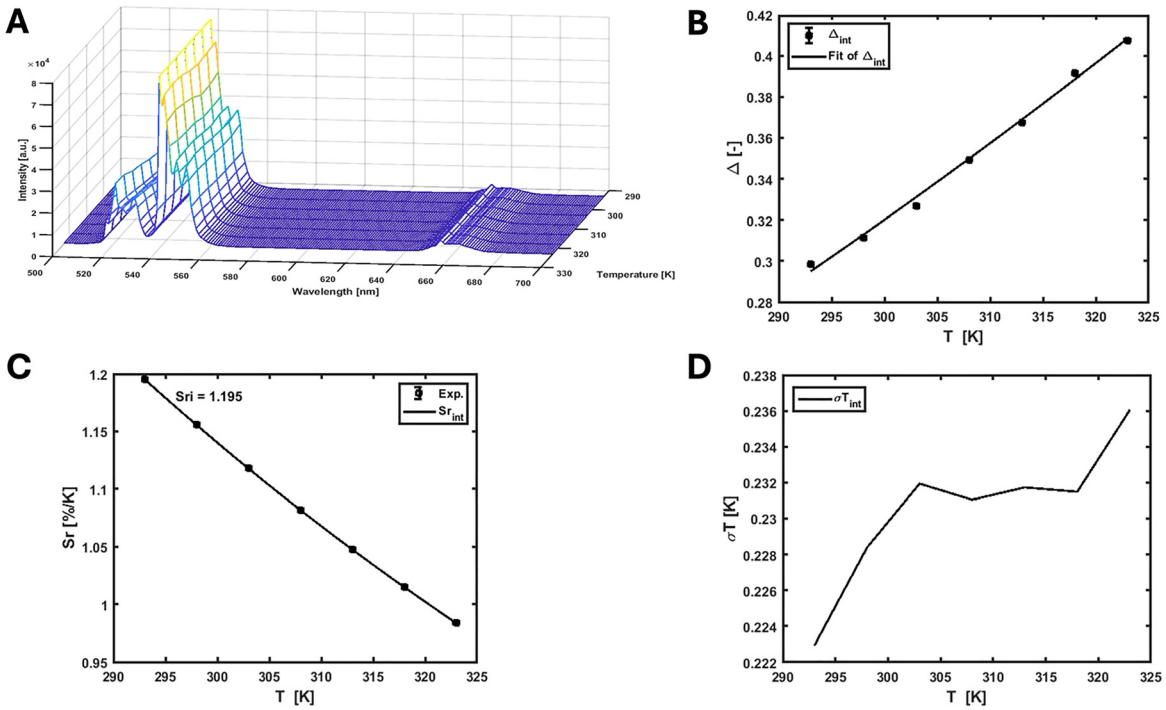

Fig. 7 (A) Emission map of $NaYF_4$:Yb,Er@SiO_2 dispersed in water, recorded across the temperature range of 293.15–323.15 K (20–50 °C) in the visible ($^2H_{11/2} \rightarrow {}^4I_{15/2}$ and $^4S_{3/2} \rightarrow {}^4I_{15/2}$) under 940 nm excitation, (B) graph showing the Δ parameter *versus* temperature. The points show the experimental Δ values, and the solid line shows the least squares fit to the experimental points. (C) Plot of the relative sensitivity (S_r) at varying temperatures. (D) Plot of the temperature uncertainty (σT) at varying temperatures.

excellent repeatability across the tested temperature range. At an excitation wavelength of 975 nm, the material maintained a repeatability of approximately 96%, while at 940 nm excitation, the repeatability was, around 99%, as calculated using eqn (8). This highlights that the material can provide stable, repeatable measurements, making it a promising candidate for non-invasive, accurate temperature monitoring in biological applications.

Temperature-dependent luminescence studies in biological tissues

To examine the influence of tissue thickness on luminescence signals, emission spectra of $NaYF_4$:Yb,Er@SiO_2-NH_2@FA were acquired through chicken breast tissue (2 mm thickness) under 975 nm and 940 nm laser excitation at physiological temperatures (20–50 °C). The tissue samples were placed on the outer walls of the sample cuvette, both at the entrance of the light through the cuvette and at its exit to simulate *in vivo* conditions (Scheme 3). As in earlier experiments NIR-I emissions from the particles were collected under 975 nm excitation, demonstrating their suitability for temperature sensing in deep tissues.

Under 975 nm excitation (1350 mW), we successfully detected NIR-I emission through the tissue, and could calculate the I_{795}/I_{840} ratio, confirming deep-tissue signal penetration. The particles exhibited strong thermometric performance with S_r = 1.138% K^{-1}, R^2 = 0.988, ΔE = 679 cm^{-1}, and σT = 0.52 K (Fig. 11A, D and Table 2), indicating good temperature responsiveness suitable for biological applications. The ability to measure signals in the NIR-I range also suggests the potential for non-invasive monitoring of temperature gradients in deep tissues, which could be significant for applications like medical diagnostics and therapeutic monitoring. However, with 940 nm excitation (547 mW, the maximum available power in our lab), unfortunately no detectable NIR-I signal was observed. This difference is likely due to the relatively lower power of the 940 nm laser, *i.e.* around 2.5 times weaker than the 975 nm one, which may have been insufficient to generate measurable NIR-I emission through the tissue, and not to the laser wavelength itself.

Furthermore, when measurements were performed through 5 mm of tissue, NIR-I emission could still be detected under

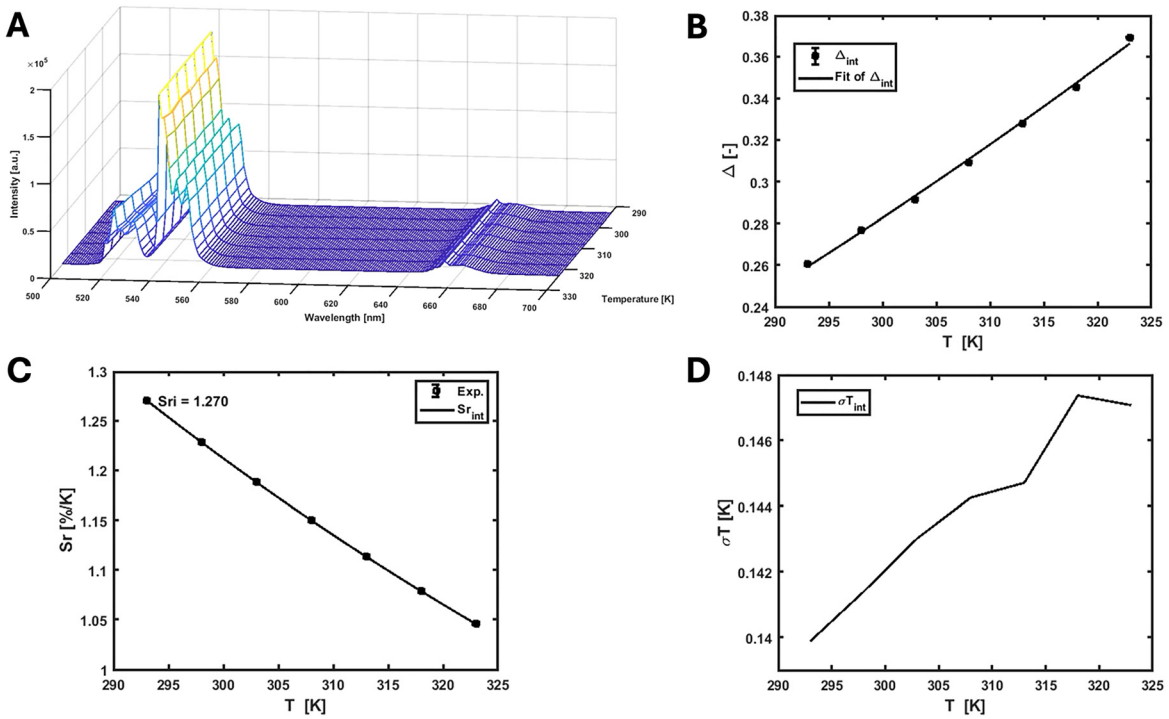

Fig. 8 (A) Emission map of $NaYF_4$:Yb,Er@SiO_2-NH_2@FA dispersed in water, recorded across the temperature range of 293.15–323.15 K (20–50 °C) in the visible region ($^2H_{11/2} \rightarrow {}^4I_{15/2}$ and $^4S_{3/2} \rightarrow {}^4I_{15/2}$) under 940 nm excitation, (B) graph showing the Δ parameter *versus* temperature. The points show the experimental Δ values, and the solid line shows the least squares fit to the experimental points. (C) Plot of the relative sensitivity (S_r) at varying temperatures. (D) Plot of the temperature uncertainty (σT) at varying temperatures.

Table 3 Thermometric parameters in the visible range under 940 nm excitation, performed in water unless otherwise specified

Compounds	R^2	ΔE (cm^{-1})	S_r (% K^{-1})	σT (K)
$NaYF_4$:18%Yb,2%Er (cyclohexane)	0.984	696	1.167	0.15
$NaYF_4$:18%Yb,2%Er@SiO_2	0.995	713	1.195	0.24
$NaYF_4$:18%Yb,2%Er@SiO_2–NH_2@FA	0.998	758	1.270	0.15
$NaYF_4$:18%Yb,2%Er@SiO_2–NH_2@FA@DOX	0.967	558	0.935	1.11

975 nm excitation, with thermometric parameters of S_r = 1.162% K^{-1}, R^2 = 0.961, ΔE = 694 cm^{-1}, and σT = 1.4 K (Fig. S13A–D). Compared to the 2 mm case, the slight decrease in R^2 and the increase in temperature uncertainty clearly indicate the expected reduction of signal quality with increasing tissue thickness. These changes are consistent with increased scattering and absorption at greater depths, which reduce the signal-to-noise ratio and thus affect the precision of temperature determination.

Drug loading and release experiments

To investigate the drug release kinetics of DOX from $NaYF_4$:Yb,Er@SiO_2-NH_2@FA particles, a standard calibration curve was first established by spectrophotometrically measuring the absorbance of DOX solutions at 480 nm across a series of known concentrations. This calibration enabled precise quantification of DOX concentrations in subsequent release studies. After loading the particles with DOX, we determined the LC% and EE% using the calibration data (Fig. S14A and B). The results indicated an LC% of approximately 39%, reflecting the proportion of DOX successfully loaded relative to the carrier material, while the EE% was determined to be about 64%, demonstrating efficient drug incorporation within the particles. These findings confirm effective DOX loading and provide a foundation for subsequent drug release studies.

The release profile of DOX from $NaYF_4$:Yb,Er@SiO_2-NH_2@FA@DOX was evaluated over 24 hours in PBS (37 °C) at physiological (pH 7.4) and acidic (pH 5.5) conditions by monitoring absorbance at 480 nm. As shown in Fig. 12A, DOX release exhibited strong pH dependence. Under neutral conditions (pH 7.4), only 4% of the drug was released after 24 hours, indicating high stability in physiological environments. In contrast, at pH 5.5, release efficiency increased six-fold, reaching 25% in the same period. Such behaviour is consistent with well-established properties of mesoporous silica systems, where pore size, pore volume, and surface chemistry strongly influence how tightly drug molecules are retained.[56–58] Moreover, When the pores are small or the surface interacts strongly with the drug molecules, diffusion becomes restricted and the release rate decreases. In contrast, larger pores or chemical surface modifications (*e.g.* grafting of amino, carboxyl or other functional groups) can improve drug adsorption, stabilize the loaded molecules, and enable more controlled or triggered release profiles.[59] These structural factors help explain why DOX remains more tightly retained under some surface conditions yet displays enhanced release under others.

To better understand the role of surface functionalization, we compared the DOX release profiles for $NaYF_4$:Yb,Er@SiO_2

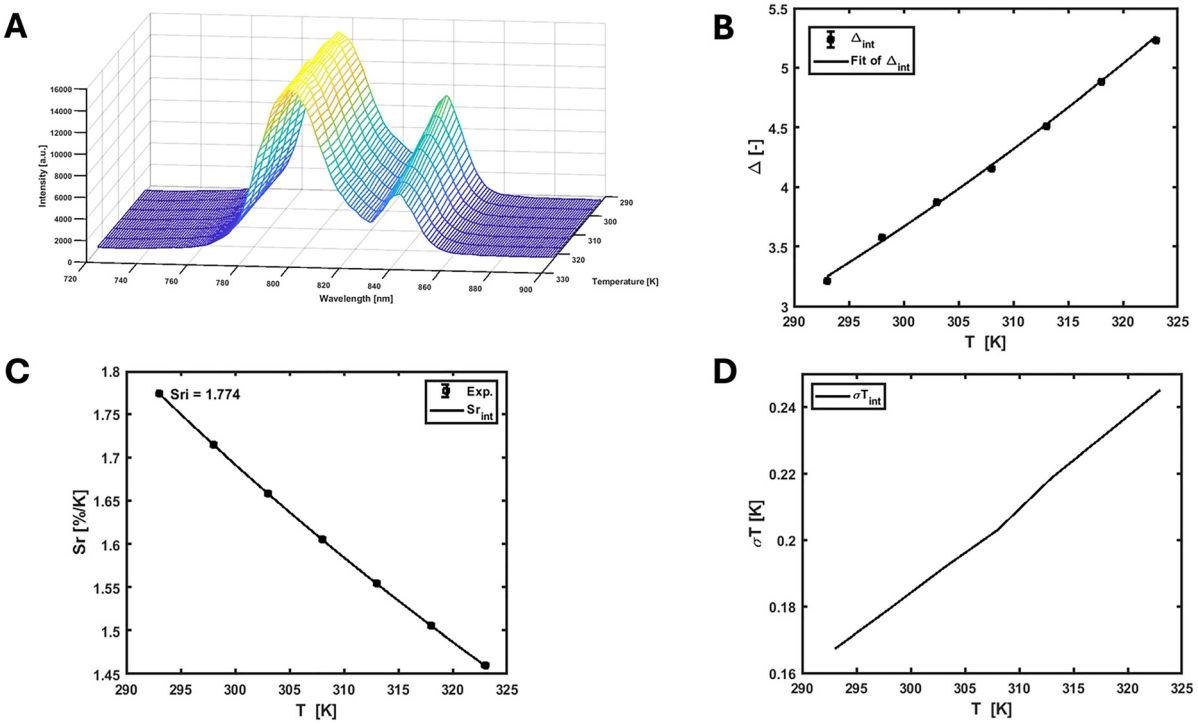

Fig. 9 (A) Emission map of $NaYF_4$:Yb,Er@SiO_2 dispersed in water, recorded across the temperature range of 293.15–323.15 K (20–50 °C) in the NIR-I ($^2H_{11/2} \rightarrow {}^4I_{13/2}$ and $^4S_{3/2} \rightarrow {}^4I_{13/2}$) region under 940 nm excitation, (B) graph showing the Δ parameter *versus* temperature. The points show the experimental Δ values, and the solid line shows the least squares fit to the experimental points. (C) Plot of the relative sensitivity (S_r) at varying temperatures. (D) Plot of the temperature uncertainty (σT) at varying temperatures.

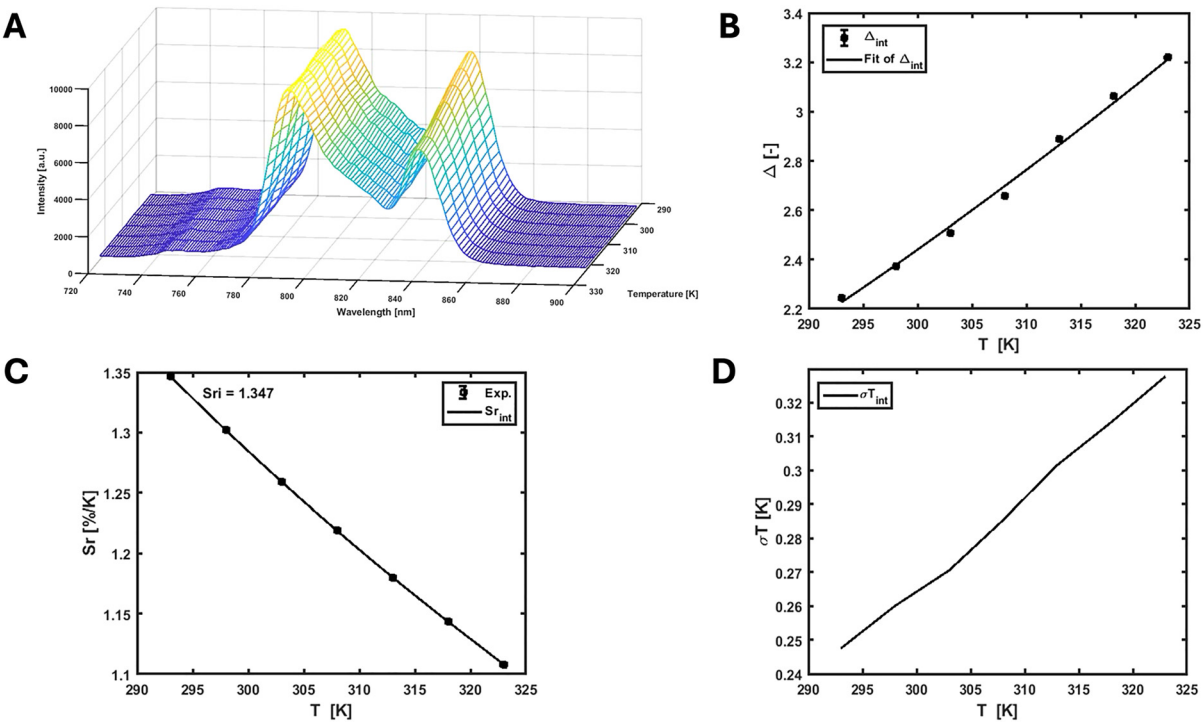

Fig. 10 (A) Emission map of $NaYF_4$:Yb,Er@SiO_2-NH_2@FA dispersed in water, recorded across the temperature range of 293.15–323.15 K (20–50 °C) in the NIR-I region ($^2H_{11/2} \rightarrow {}^4I_{13/2}$ and $^4S_{3/2} \rightarrow {}^4I_{13/2}$) under 940 nm excitation, (B) graph showing the Δ parameter *versus* temperature. The points show the experimental Δ values, and the solid line shows the least squares fit to the experimental points. (C) Plot of the relative sensitivity (S_r) at varying temperatures. (D) Plot of the temperature uncertainty (σT) at varying temperatures.

Table 4 Thermometric parameters in the NIR-I range under 940 nm excitation, performed in water unless otherwise specified

Compounds	R^2	ΔE (cm^{-1})	S_r (% K^{-1})	σT (K)
$NaYF_4$:18%Yb,2%Er (cyclohexane)	0.993	613	1.027	0.24
$NaYF_4$:18%Yb,2%Er@SiO_2	0.998	1058	1.774	0.24
$NaYF_4$:18%Yb,2%Er@SiO_2–NH_2@FA	0.995	805	1.347	0.33
$NaYF_4$:18%Yb,2%Er@SiO_2–NH_2@FA@DOX [a]	—	—	—	—

[a] Indicates that the fitting was not sufficient to ensure reliable analysis; therefore, the thermometric parameters were not evaluated further.

and $NaYF_4$:Yb,Er@SiO_2-NH_2 particles under acidic conditions (pH 5.5) to simulate the tumor microenvironment (Fig. 12B). The results demonstrated significantly slower release rates in both cases. $NaYF_4$:Yb,Er@SiO_2 released approximately 11% of the loaded DOX after 24 h, while $NaYF_4$:Yb,Er@SiO_2-NH_2, modified with amine groups through APTES treatment, showed a similarly low release of about 10%. The limited release may be attributed to strong electrostatic interactions between the positively charged DOX molecules and the negatively charged silica surface or amine-modified surface, which likely restricts drug diffusion. These findings suggest that, in the absence of FA modification, the particles retain DOX more tightly, leading to slower drug release. However, when FA is conjugated to the particles, the release is faster and more responsive to acidic conditions. This is because the FA modification reduces electrostatic interactions, enabling the drug to be released more easily under acidic conditions. This enhanced release profile could improve the efficiency of targeted drug delivery, especially for cancer therapies, by ensuring more controlled and localized drug release at the tumor site. In this way, folic acid plays a crucial dual role in drug delivery systems. In addition to its well-established function in targeting specific tumor cells through the overexpression of folate receptors, it also enhances drug release, making it an effective agent for both targeting and controlled drug delivery. The overall comparative results confirm the pH-responsive nature of the drug release, consistent with observations reported in various other systems.[5,6,11,23]

Table 5 Relative temperature sensitivities of various nanothermometers operating in the NIR-I region compared with results obtained in our work

Compounds	λ_{ex} (nm)	λ_{em} (nm)	Temperature range (K)	S_r (% K^{-1})	Ref.
YF_3:Yb^{3+},Er^{3+}	980	793, 840	293–473	0.98 ± 0.10	14
$NaYF_4$:Er^{3+} glassy matrix	488	790, 850	293–720	1.2	15
Y_2O_3:Er^{3+}	800	800	293–353	2.02 ± 0.06	49
$NaYF_4$:Er^{3+}	517	837, 980	113–443	2.15	50
$PbZrTiO_3$:Yb^{3+},Er^{3+}	980	858, 878	300–673	1.56	17
YVO_4:Nd^{3+}	532	808, 880	123–873	1.5	51
YF_3:Yb^{3+},Tm^{3+}	975	800, 940	300–345	0.8	52
α-$NaYF_4$:Yb^{3+},Tm^{3+}@CaF_2	980	802, 820	313–373	0.43	53
Fluoroborontellurite glass:Nd^{3+}	532	820, 890	280–480	1.58	54
$YNbO_4$:Nd^{3+}	752	893, 930	303–473	0.28	55
$NaYF_4$:Yb,Er@SiO_2	975	795, 840	293–323	1.195	Our work
$NaYF_4$:Yb,Er@SiO_2	940	795, 840	293–353	1.454	Our work

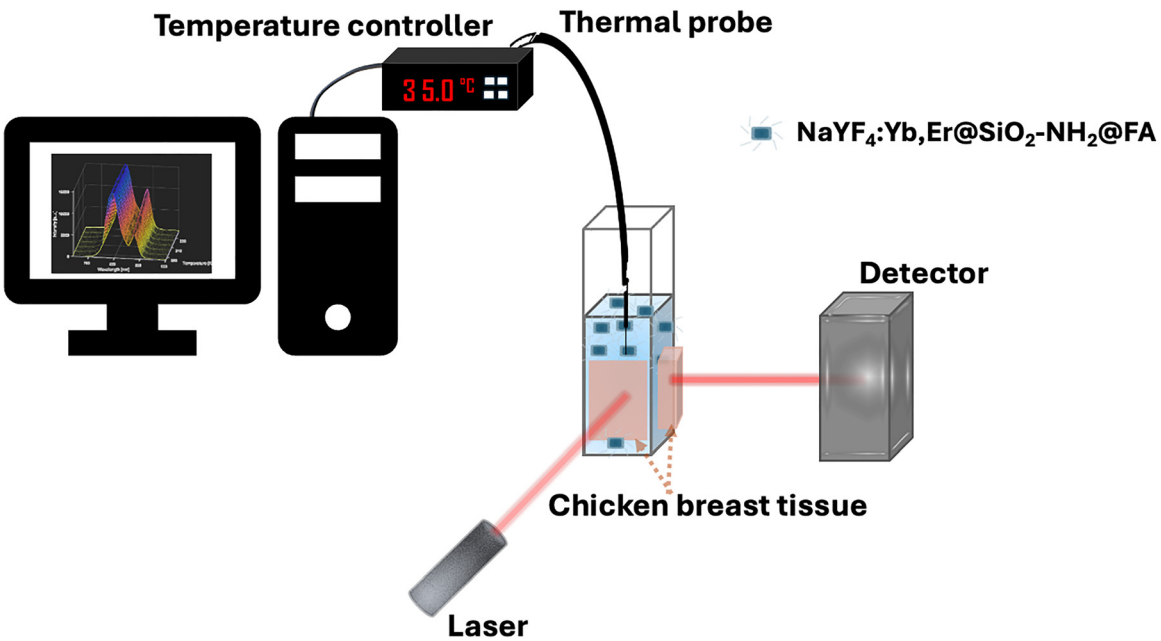

Scheme 3 Schematic visualization of the experimental setup for temperature measurements carried out through chicken breast tissue.

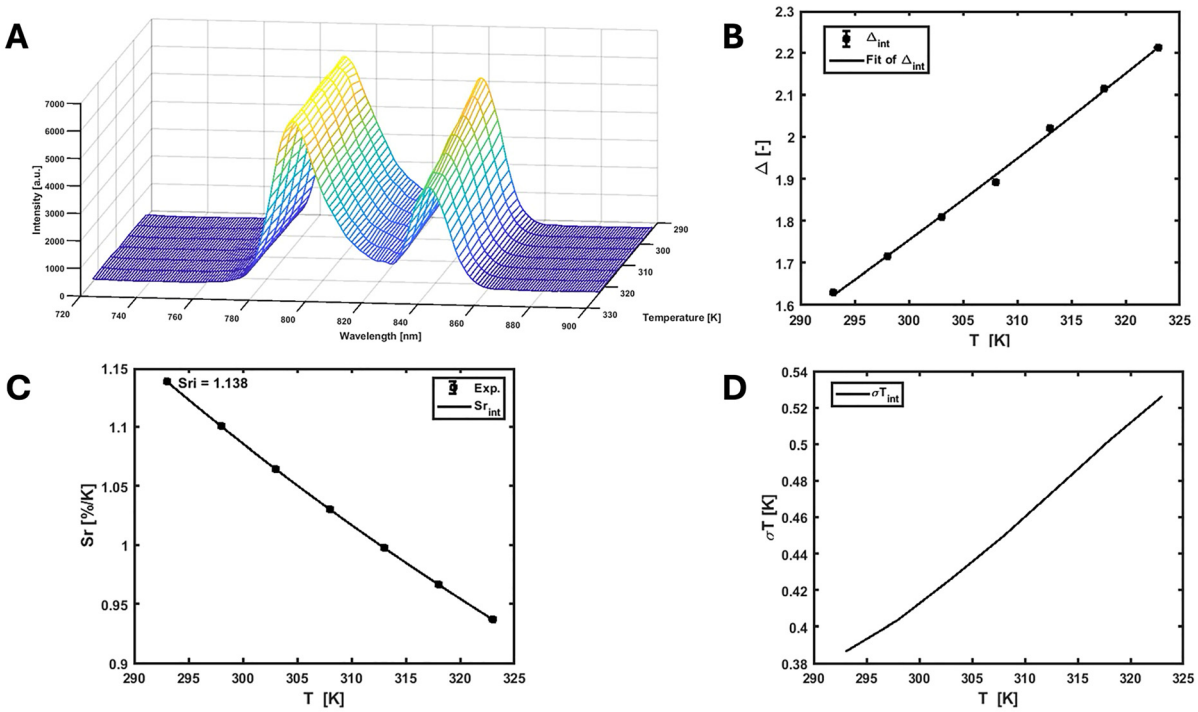

Fig. 11 (A) Emission map of $NaYF_4$:Yb,Er@SiO_2-NH_2@FA dispersed in water, recorded through chicken breast tissue (2 mm thickness) across the temperature range of 293.15–323.15 K (20–50 °C) in the NIR-I region ($^2H_{11/2} \rightarrow {}^4I_{13/2}$ and $^4S_{3/2} \rightarrow {}^4I_{13/2}$) under 975 nm excitation, (B) graph showing the Δ parameter *versus* temperature. The points show the experimental Δ values, and the solid line shows the least squares fit to the experimental points. (C) Plot of the relative sensitivity (S_r) at varying temperatures. (D) Plot of the temperature uncertainty (σT) at varying temperatures.

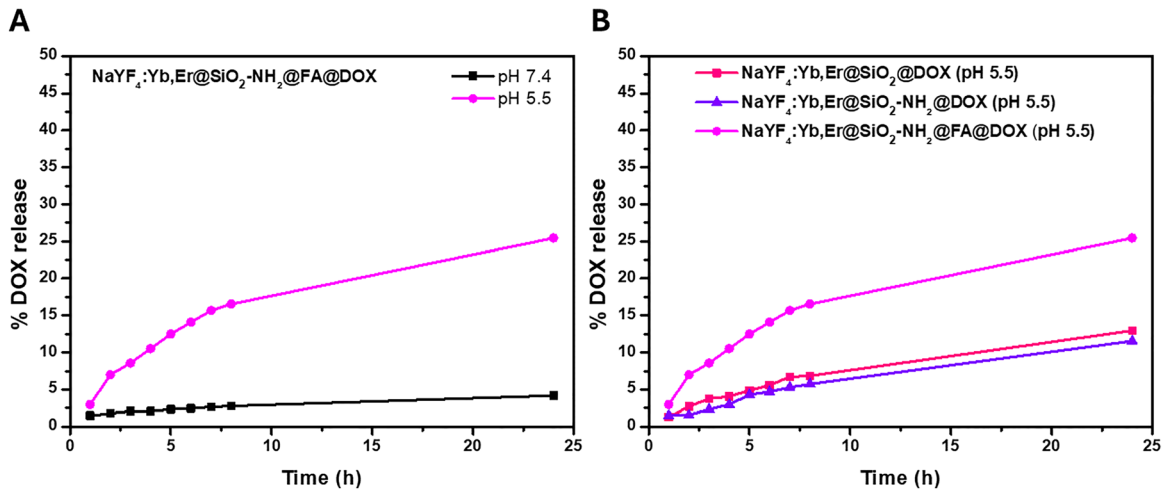

Fig. 12 DOX release profiles of $NaYF_4$:Yb,Er@SiO_2-NH_2@FA@DOX monitored at two different pH values 5.5 and 7.4, (B) comparison of DOX release from $NaYF_4$:Yb,Er@SiO_2, $NaYF_4$:Yb,Er@SiO_2-NH_2, and $NaYF_4$:Yb,Er@SiO_2-NH_2@FA at pH 5.5.

To further elucidate the mechanism of DOX release, the experimental release data were fitted using the Higuchi kinetic model, expressed as (eqn (9)):

$$\frac{M_t}{M_\infty} = k_H \cdot \sqrt{t} \quad (9)$$

where M_t is the amount of drug released at time t, M_∞ is the total amount of drug released at equilibrium, and k_H is the Higuchi release constant describing diffusion through the matrix.

Linear regression yielded k_H values of 0.187, 0.176, and 0.212 for $NaYF_4$:Yb,Er@SiO_2@DOX, $NaYF_4$:Yb,Er@SiO_2-NH_2@DOX, and $NaYF_4$:Yb,Er@SiO_2-NH_2@FA@DOX, respectively, with excellent linearity (R^2 = 0.986, 0.970, 0.992) (Fig. S15A–C). This confirms that DOX release is predominantly diffusion-controlled, governed by the transport of molecules through the silica shell. The relatively slow release (25% after 24 h at pH 5.5) is consistent with previous reports showing restricted diffusion of DOX from silica matrices due to drug entrapment within the inner cavity

and limited pore accessibility.[35,60] It can be noticed that FA functionalization increases the Higuchi constant, indicating enhanced DOX mobility at the particle surface and improved release efficiency (Table S2).

In addition, the initial segment of the release curves $\left(\frac{M_t}{M_\infty} < 0.6\right)$ was fitted to the Korsmeyer–Peppas model $\left(\frac{M_t}{M_\infty} = k_p \cdot t^n\right)$, where t is the release time, k_p is the release constant and n is the diffusional exponent. The obtained n values were 0.78, 0.74 and 0.84 for $NaYF_4$:Yb,Er@SiO_2@DOX, $NaYF_4$:Yb,Er@SiO_2-NH_2@DOX, $NaYF_4$:Yb,Er@SiO_2-NH_2@FA@DOX, respectively (R^2 = 0.91–0.98), which fall in the range $0.43 < n < 0.85$ characteristic of anomalous but diffusion-dominated transport for spherical systems (Table S2).[61] These results are in good agreement with the Higuchi analysis and further confirm that DOX release is controlled primarily by diffusion through the silica shell, with FA functionalization slightly enhancing the release rate.

To evaluate whether DOX loading affects the thermometric performance of the material, we systematically investigated the temperature-sensing capabilities of $NaYF_4$:Yb,Er@SiO_2-NH_2@FA@DOX particles across both the green and NIR-I spectral regions. Under 975 nm excitation, upon DOX loading, we observed a significant decrease in the green upconversion emission intensity of $NaYF_4$:Yb,Er@SiO_2-NH_2@FA@DOX, while the red emission around 655 nm remained strongly pronounced (Fig. S9). By monitoring the temperature-dependent intensity ratio of the $^2H_{11/2} \rightarrow {}^4I_{15/2}$ and $^4S_{3/2} \rightarrow {}^4I_{15/2}$ transitions, we calculated a thermometric parameter (Δ) that increased gradually with temperature, yielding ΔE of 564 cm^{-1}, R^2 = 0.988, S_r of 0.946% K^{-1}, and σT of 0.67 K (Fig. S10A–D). These results confirm that, although the absolute emission intensity in the green region decreases with DOX loading, the thermometric performance remains reliable. This stability arises because the thermometric behavior relies on the emission intensity ratio of the Er^{3+} thermally coupled levels, which follows a Boltzmann distribution and is not significantly affected by surface functionalization.[6] We further evaluated the thermometric performance in the NIR-I region under the same excitation conditions, obtaining a comparable ΔE of 607.50 cm^{-1}, R^2 = 0.988, S_r = 1.018% K^{-1}, and σT = 0.25 K (Fig. S11A–D), indicating minimal influence of DOX on performance in this spectral range as well.

Furthermore, we investigated the thermometric performance of the $NaYF_4$:Yb,Er@SiO_2-NH_2@FA@DOX under 940 nm excitation to evaluate its potential as an alternative excitation source. In the visible emission range, the system demonstrated reliable thermometric behavior, with a calculated ΔE of 558 cm^{-1}, R^2 of 0.967, S_r of 0.935% K^{-1}, and σT of 1.11 K (Fig. S12A–D). Although emission in the NIR-I region was also observed under 940 nm excitation, the fit quality was insufficient for reliable evaluation of thermometric parameters. This limitation we observe can be attributed to the lower power output of the 940 nm laser (547 mW) compared to the

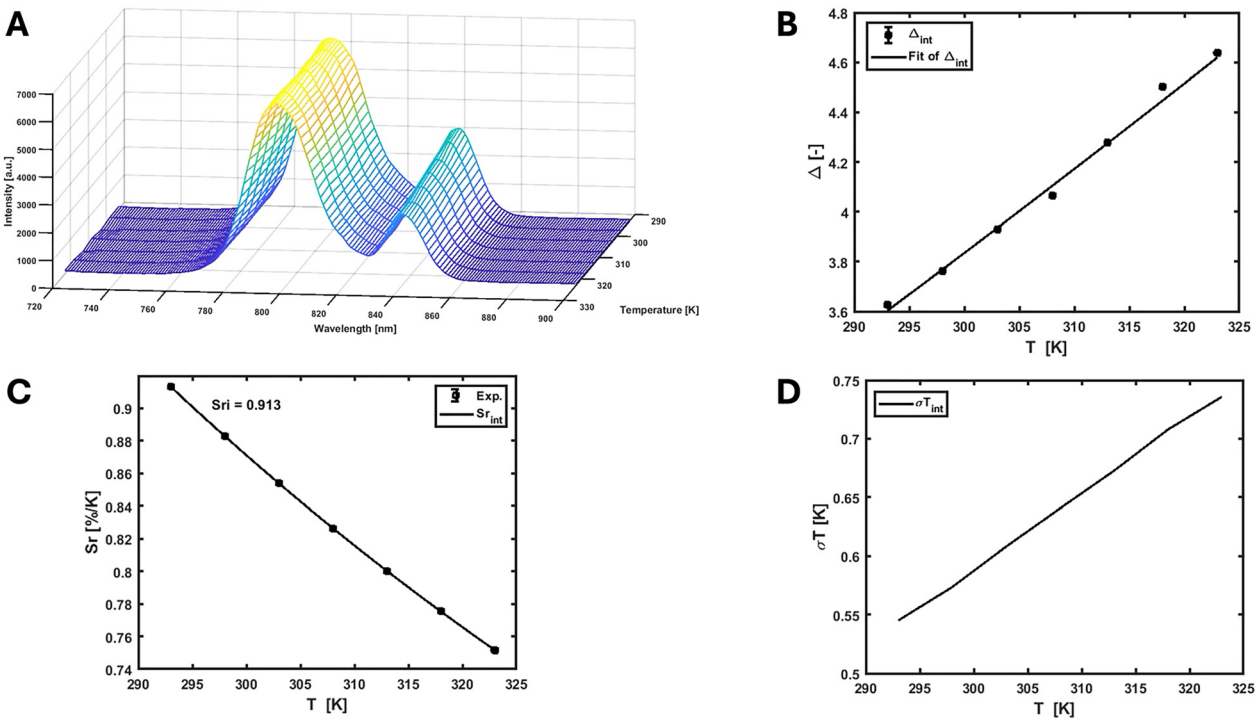

Fig. 13 Emission map of $NaYF_4$:Yb,Er@SiO_2-NH_2@FA@DOX dispersed in water, recorded through chicken breast tissue (2 mm at light entrance and 2 mm at light exit) across the temperature range of 293.15–323.15 K (20–50 °C) in the NIR-I region ($^2H_{11/2} \rightarrow {}^4I_{13/2}$ and $^4S_{3/2} \rightarrow {}^4I_{13/2}$) under 975 nm excitation, (B) graph showing the Δ parameter *versus* temperature. The points show the experimental Δ values, and the solid line shows the least squares fit to the experimental points. (C) Plot of the relative sensitivity (S_r) at varying temperatures. (D) Plot of the temperature uncertainty (σT) at varying temperatures.

975 nm laser (1350 mW), which results in less efficient excitation of Yb^{3+} ions and weaker energy transfer to Er^{3+}.

To further evaluate the impact of DOX loading on deep-tissue thermometric performance, we examined the NIR-I emission of $NaYF_4$:Yb,Er@SiO_2-NH_2@FA@DOX under both 975 nm and 940 nm excitation through 2 mm thick chicken breast tissue, across a physiological temperature range (20–50 °C). Under 975 nm excitation, the material exhibited strong NIR-I emission and good thermometric performance, with R^2 = 0.993, S_r = 0.913% K^{-1}, ΔE = 544.93 cm^{-1}, and σT = 0.75 K (Fig. 13A–D). However, under 940 nm excitation, no measurable signal was detected in the NIR-I region, indicating that this excitation wavelength is insufficient for effective thermometric readout through tissue in DOX-loaded samples. As previously mentioned, the difference in excitation efficiency can account for the lack of observable signal under 940 nm excitation. All corresponding values are summarized in Tables 1–4.

PrestoBlue HS cell viability assay

To assess the cytotoxicity and anticancer potential of the $NaYF_4$:Yb,Er@SiO_2-NH_2@FA and $NaYF_4$:Yb,Er@SiO_2-NH_2@FA@DOX particles, we evaluated their cytotoxicity on NHDF and HeLa cells (a cervical cancer cell line) at varying concentrations (0 [control], 1, 2.5, 5, 10, 25, 50, 200 and 500 μg mL^{-1}) over 24 hours. To evaluate the cytotoxicity effect of the particles themselves without DOX loading, the cytotoxicity results of the $NaYF_4$:Yb,Er@SiO_2-NH_2@FA particles, as overviewed in the bar chart (Fig. S16A and B), demonstrate no substantial toxicity toward both NHDF and HeLa cells, where cell viability remained close to 90–100% across concentrations from 1 to 50 μg mL^{-1}, indicating excellent biocompatibility. A noticeable reduction in cell viability was observed only at very high concentrations ($\geq$200 μg mL^{-1}). In NHDF cells, viability decreased to approximately 35% at 200 μg mL^{-1} and dropped further at 500 μg mL^{-1}, while HeLa cells showed a more pronounced decrease at these highest doses. These findings suggest that while the particles are generally biocompatible, their cytotoxic effects become significant at elevated concentrations. This mildly beneficial cell viability effect at relatively low concentrations has been observed previously in MCF7 cells as a model cancer cell line with overexpressed folate receptors in the cell membranes, with FA-functionalized polymer-stabilized Fe_3O_4 particles.[62] This observation could be due to a slightly favourable nutrient effect of the folic acid which participates in vital cellular metabolic pathways,[63] and possibly due to the simultaneous activation of certain cell internalization pathways which promote cell proliferation. Another evidence of this is demonstrated in a study on stress caused by low folate content which has been found to promote cancer malignancy in cancer stem cell phenotypes such as lung cancer.[64]

The anticancer performance of the particles was assessed by comparing DOX-loaded $NaYF_4$:Yb,Er@SiO_2-NH_2@FA@DOX with free DOX in NHDF and HeLa cells over a concentration range of 0–500 μg mL^{-1} (Fig. 14A and B). For comparisons between DOX-loaded $NaYF_4$:Yb,Er@SiO_2-NH_2@FA@DOX particles and free DOX, the concentrations shown in the cytotoxicity plots were expressed as nanoparticle-equivalent doses. Based on the experimentally determined DOX loading capacity of the $NaYF_4$:Yb,Er@SiO_2-NH_2@FA particles (39%), the actual concentration of free DOX corresponds to 39% of the nominal value indicated on the *x*-axis. For example, an indicated concentration of 10 μg mL^{-1} represents an actual free DOX concentration of 3.9 μg mL^{-1}. The concentrations were kept consistent in the graphs allow a direct comparison between a given nanoparticle dose and the estimated amount of DOX delivered by that dose, enabling evaluation of the therapeutic performance of the nanoparticle delivery system relative to its drug payload.

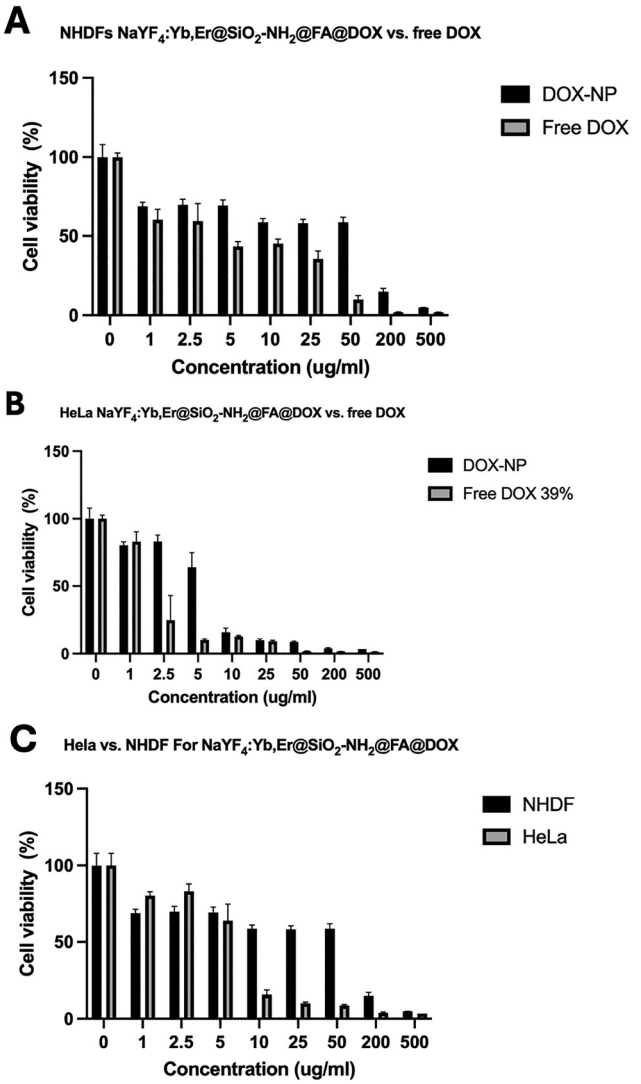

Fig. 14 Bar graph (mean + SD) of cytotoxicity test results obtained for the tested DOX loaded $NaYF_4$:Yb,Er@SiO_2-NH_2@FA@DOX particles (DOX-NP) compared with free DOX on the chosen NHDF and HeLa cell line models. (A) Cytotoxicity of DOX-NP *versus* free DOX in NHDF cells, (B) cytotoxicity of DOX-NP *versus* free DOX in HeLa cells and (C) comparative cytotoxicity of DOX-NP in NHDF *versus* HeLa cells across the same concentration range. A nonparametric statistical analysis was conducted, employing the Mann–Whitney-Wilcoxon test to investigate significant differences between the control media and any other concentration group median of a tested sample. [a] Free DOX concentrations correspond to 39% of the indicated nanoparticle-equivalent dose, based on the measured DOX loading capacity (LC%) as described in the Drug Loading and Release Experiments.

DOX-loaded $NaYF_4$:Yb,Er@SiO_2-NH_2@FA@DOX particles caused a concentration-dependent reduction in cell viability in both NHDF and HeLa cells, confirming effective intracellular delivery of DOX and its resulting cytotoxicity. However, at equivalent nominal concentrations, free DOX consistently produced greater cytotoxicity than the DOX-loaded particles, especially at lower and intermediate concentration. This outcome is expected because free DOX diffuses rapidly into cells and exerts its cytotoxic effect immediately, whereas DOX encapsulated within particles requires cellular uptake followed by drug release, leading to a more gradual onset of toxicity. In HeLa cells, the DOX loaded $NaYF_4$:Yb,Er@SiO_2-NH_2@FA@DOX particles maintained strong cytotoxicity across the tested concentration range, consistent with effective folate-receptor-assisted internalization. However, NHDF cells displayed comparatively higher viability under the same treatment conditions, suggesting reduced nonspecific toxicity and a degree of preferential action toward cancer cells.

A direct comparison between NHDF and HeLa cells treated with $NaYF_4$:Yb,Er@SiO_2-NH_2@FA@DOX (Fig. 14C) further confirmed the greater susceptibility of HeLa cells, consistent with folate receptor overexpression on cancer cell membranes. At concentrations $\geq$10 μg mL^{-1}, HeLa cell viability dropped sharply, whereas NHDF cells retained moderate viability, supporting the selective anticancer potential of the FA-targeted conjugate.

To study the intracellular uptake of DOX-loaded particles in HeLa cells, the cells were first stained with CFSE following the manufacturer's instructions. They were then seeded into 8-well glass-bottom Ibidi slides and allowed to adhere overnight. Subsequently, the cells were treated with 10 μg mL^{-1} DOX-loaded $NaYF_4$:Yb,Er@SiO_2-NH_2@FA@DOX particles for 4 hours, washed twice, and fixed with 4% PFA for 15 minutes. After additional washing, the cells were kept in PBS. Imaging was performed using the Confocal.NL system, with the 488-nm channel used to visualize the cell membrane and the 561-nm channel to detect the nanoparticles. As shown in Fig. 15, the green fluorescence signal (488 nm channel) corresponds to the CFSE-stained HeLa cells, while the red fluorescence signal (561 nm channel) displays the DOX-loaded particles, $NaYF_4$:Yb,Er@SiO_2-NH_2@FA@DOX. The presence of red signals within the three-dimensional morphology of the green-labeled HeLa cells confirms the cellular internalization of the $NaYF_4$:Yb,Er@SiO_2-NH_2@FA@DOX particles. This is shown through the given z-slices of the orthogonal projection collected simultaneously during the microscopy scan.

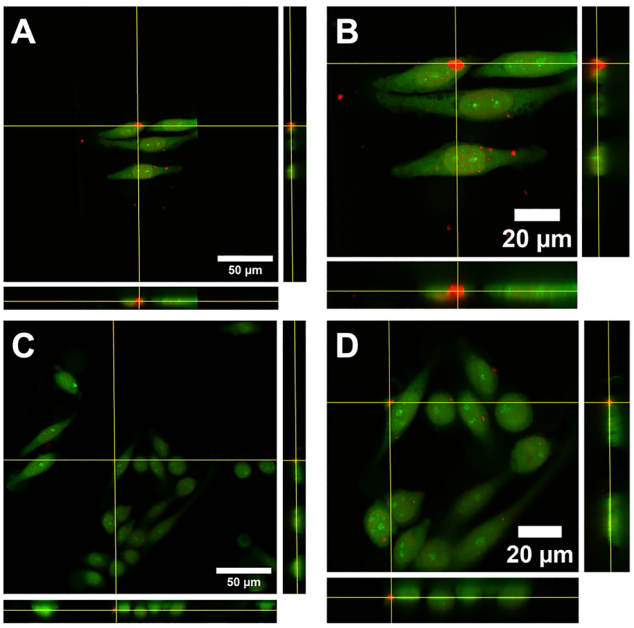

Fig. 15 Orthogonal view (*z*-slices) of confocal microscopy images (center: original *x*–*y*, bottom: *x*–*z*, and side: *y*–*z* planes) portraying the 3D morphology of the HeLa cells (stained with green-emitting CFSE), incubated with red-emitting DOX-loaded nanoparticles, $NaYF_4$:Yb,Er@SiO_2-NH_2@FA at a concentration of 10 μg mL^{-1}. Both regular (A) and (C) and corresponding zoomed-in (B) and (D) orthogonal views are shown. Yellow lines indicate the location of *z*-slices/projection planes within the scan.

Conclusion

In summary, we have successfully synthesized cuboidal $NaYF_4$:Yb,Er particles and engineered them for biomedical applications through a series of surface modifications. The transformation from hydrophobic to hydrophilic surfaces *via* mesoporous silica coating enhanced their aqueous dispersibility, stability, and biocompatibility. Subsequent functionalization with folic acid and loading with DOX enabled pH-responsive drug release, while the upconversion luminescence properties allowed for ratiometric temperature sensing in both the visible and NIR-I regions under dual NIR excitation at 975 nm and 940 nm. Additionally, the relative sensitivity S_r was quantified to evaluate the thermometric performance of the system. The ability to measure temperatures in the NIR-I regions provides a significant advantage for applications in biological tissues, where deeper tissue penetration and minimized interference from biological autofluorescence are crucial. Cyclic tests performed in the NIR-I region confirmed the stability and reliability of the temperature sensing over repeated measurements. Furthermore, our system effectively integrated both thermometric and drug delivery capabilities, demonstrating pH-responsive drug release and accurate thermal readouts through biological tissue models (chicken breast tissue), highlighting its potential as a multifunctional platform for cancer therapy, bioimaging, and localized thermometry.

Author contributions

The manuscript was written through contributions of all authors. All authors have given approval to the final version of the manuscript.

Conflicts of interest

There are no conflicts to declare.

Data availability

The data supporting this article have been included, including particle size distribution, zeta potential, luminescence and thermometry measurements, cycle test, DOX calibration curves, release kinetic fitting and cytotoxicity data, as part of the supplementary information (SI). Supplementary information is available. See DOI: https://doi.org/10.1039/d5tb02109j.

Acknowledgements

This work is supported by funding from the European Research Council (ERC) under the European Union's Horizon 2020 research and innovation program (Grant Agreement No. 945945). KVH thanks the Special Research Fund (BOF) – UGent (BOF/24J/2023/084). We acknowledge the support of BOF-UGent (BOF23/GOA/029). The work was supported by the European Union under the Marie Sklodowska-Curie grant agreement no. 101072861. Views are of the authors only. TEM measurements were performed at the UGent TEM Core Facility.

References

1 J. Zhou, Q. Liu, W. Feng, Y. Sun and F. Li, *Chem. Rev.*, 2015, **115**, 395–465.
2 C. Li and J. Lin, *J. Mater. Chem.*, 2010, **20**, 6831–6847.
3 L.-D. Sun, Y.-F. Wang and C.-H. Yan, *Acc. Chem. Res.*, 2014, **47**, 1001–1009.
4 B. Zheng, J. Fan, B. Chen, X. Qin, J. Wang, F. Wang, R. Deng and X. Liu, *Chem. Rev.*, 2022, **122**, 5519–5603.
5 S. Mohanty, J. García-Balduz, A. E. Alici, S. Premcheska, M. Lederer, A. Skirtach, K. Van Hecke and A. M. Kaczmarek, *ACS Appl. Mater. Interfaces*, 2024, **16**, 57580–57595.
6 S. Mohanty, M. Lederer, S. Premcheska, H. Rijckaert, K. De Buysser, E. Bruneel, A. Skirtach, K. Van Hecke and A. M. Kaczmarek, *J. Mater. Chem. C*, 2024, **12**, 11785–11802.
7 S. A. Wade, S. F. Collins and G. W. Baxter, *J. Appl. Phys.*, 2003, **94**, 4743–4756.
8 R. Naccache, Q. Yu and J. A. Capobianco, *Adv. Opt. Mater.*, 2015, **3**, 482–509.
9 S. P. Tiwari, S. K. Maurya, R. S. Yadav, A. Kumar, V. Kumar, M.-F. Joubert and H. C. Swart, *J. Vac. Sci. Technol., B: Nanotechnol. Microelectron.: Mater., Process., Meas., Phenom.*, 2018, **36**, 060801.
10 M. Suta, *Nanoscale*, 2025, **17**, 7091–7099.
11 S. Mohanty, S. Premcheska, J. Verduijn, H. Rijckaert, A. G. Skirtach, K. Van Hecke and A. M. Kaczmarek, *RSC Adv.*, 2022, **12**, 33239–33250.
12 H. Suo, C. Guo, J. Zheng, B. Zhou, C. Ma, X. Zhao, T. Li, P. Guo and E. M. Goldys, *ACS Appl. Mater. Interfaces*, 2016, **8**, 30312–30319.
13 M. Jia, Z. Sun, F. Lin, B. Hou, X. Li, M. Zhang, H. Wang, Y. Xu and Z. Fu, *J. Phys. Chem. Lett.*, 2019, **10**, 5786–5790.
14 A. Ćirić, J. Aleksić, T. Barudžija, Ž. Antić, V. Đorđević, M. Medić, J. Periša, I. Zeković, M. Mitrić and M. D. Dramićanin, *Nanomaterials*, 2020, **10**, 627.
15 S. F. León-Luis, U. R. Rodríguez-Mendoza, P. Haro-González, I. R. Martín and V. Lavín, *Sens. Actuators, B*, 2012, **174**, 176–186.
16 A. M. Kaczmarek, M. Suta, H. Rijckaert, A. Abalymov, I. Van Driessche, A. G. Skirtach, A. Meijerink and P. Van Der Voort, *Adv. Funct. Mater.*, 2020, **30**, 2003101.
17 P. P. Sukul, Y. Singh and H. Swart, *Phys. Chem. Chem. Phys.*, 2025, **27**, 270–282.
18 D. L. Silva, R. S. Pugina and J. M. A. Caiut, *J. Lumin.*, 2022, **243**, 118639.
19 K. Xue, C. Wang, J. Wang, S. Lv, B. Hao, C. Zhu and B. Z. Tang, *J. Am. Chem. Soc.*, 2021, **143**, 14147–14157.
20 H. Suo, X. Zhao, Z. Zhang, R. Shi, Y. Wu, J. Xiang and C. Guo, *Nanoscale*, 2018, **10**, 9245–9251.
21 J. Cai, X. Wei, F. Hu, Z. Cao, L. Zhao, Y. Chen, C. Duan and M. Yin, *Ceram. Int.*, 2016, **42**, 13990–13995.
22 M. Quintanilla, E. Cantelar, F. Cussó, M. Villegas and A. C. Caballero, *Appl. Phys. Express*, 2011, **4**, 022601.
23 H. Tonbul, A. Sahin, E. Tavukcuoglu, G. Ultav, S. Akbas, Y. Aktas, G. Esendaglı and Y. Capan, *J. Drug Delivery Sci. Technol.*, 2021, **63**, 102535.
24 D. Chávez-García, K. Juárez-Moreno, C. H. Campos, E. Tejeda, J. B. Alderete and G. A. Hirata, *J. Mater. Sci.*, 2018, **53**, 6665–6680.
25 U. Luesakul, S. Komenek, S. Puthong and N. Muangsin, *Carbohydr. Polym.*, 2016, **153**, 435–444.
26 G. Tian, W. Ren, L. Yan, S. Jian, Z. Gu, L. Zhou, S. Jin, W. Yin, S. Li and Y. Zhao, *Small*, 2013, **9**, 1929–1938.
27 D. Zhang, L. Wei, M. Zhong, L. Xiao, H.-W. Li and J. Wang, *Chem. Sci.*, 2018, **9**, 5260–5269.
28 C. I. Crucho, *Appl. Mater. Today*, 2024, **38**, 102179.
29 M. Rajotia, A. Yadav, V. K. Saroj and S. Panda, *RSC Sustainability*, 2026, DOI: 10.1039/D5SU00741K.
30 J.-N. Liu, W.-B. Bu and J.-L. Shi, *Acc. Chem. Res.*, 2015, **48**, 1797–1805.
31 V. Bastos, P. Oskoei, E. Andresen, M. I. Saleh, B. Rühle, U. Resch-Genger and H. Oliveira, *Sci. Rep.*, 2022, **12**, 3770.
32 Y. Liu, M. Zhao, M. Zhang, B. Yang, Y.-K. Qi and Q. Fu, *Mater. Today Bio*, 2025, **34**, 102223.
33 M. Moritz and M. Geszke-Moritz, *Pharmaceutics*, 2022, **14**, 1542.
34 A. M. Kaczmarek, R. Van Deun and M. K. Kaczmarek, *Sens. Actuators, B*, 2018, **273**, 696–702.
35 H. Rijckaert, S. Mohanty, J. Verduijn, M. Lederer, B. Laforce, L. Vincze, A. Skirtach, K. Van Hecke and A. M. Kaczmarek, *J. Mater. Chem. C*, 2022, **10**, 10574–10585.
36 J. Lai, B. P. Shah, Y. Zhang, L. Yang and K.-B. Lee, *ACS Nano*, 2015, **9**, 5234–5245.
37 L. T. Nguyen and R. J. Cava, *Chem. Rev.*, 2020, **121**, 2935–2965.
38 R. Shi, C. D. Brites and L. D. Carlos, *Nanoscale*, 2021, **13**, 19771–19782.
39 K. W. Krämer, D. Biner, G. Frei, H. U. Güdel, M. P. Hehlen and S. R. Lüthi, *Chem. Mater.*, 2004, **16**, 1244–1251.
40 G. Chen, H. Qiu, P. N. Prasad and X. Chen, *Chem. Rev.*, 2014, **114**, 5161–5214.

41 S. Mohanty and A. M. Kaczmarek, *Chem. Soc. Rev.*, 2022, **51**, 6893–6908.
42 K. W. Trzaskus, S. L. Lee, W. M. de Vos, A. Kemperman and K. Nijmeijer, *J. Colloid Interface Sci.*, 2017, **506**, 308–318.
43 L. Lyu, H. Cheong, X. Ai, W. Zhang, J. Li, H. Yang, J. Lin and B. Xing, *NPG Asia Mater.*, 2018, **10**, 685–702.
44 B. Bendel and M. Suta, *J. Mater. Chem. C*, 2022, **10**, 13805–13814.
45 M. Suta and A. Meijerink, *Adv. Theory Simul.*, 2020, **3**, 2000176.
46 L. Zheng, X. Huang, J. Zhong, Z. Wang and X. Cheng, *RSC Adv.*, 2021, **11**, 3981–3989.
47 G. Xiang, Q. Xia, X. Liu, Y. Wang, S. Jiang, L. Li, X. Zhou, L. Ma, X. Wang and J. Zhang, *Nanoscale*, 2021, **13**, 7161–7168.
48 D. T. Klier and M. U. Kumke, *RSC Adv.*, 2015, **5**, 67149–67156.
49 A. S. Laia, A. C. Brandão-Silva, M. A. Gomes, Z. S. Macedo, M. E. Valério, J. J. Rodrigues Jr and M. A. Alencar, *J. Alloys Compd.*, 2022, **926**, 166816.
50 F. Zhuohong, L. Lin, W. Zhezhe and Z. Zhiqiang, *J. Lumin.*, 2020, **221**, 117005.
51 A. Kalinichev, M. Kurochkin, E. Golyeva, A. Kurochkin, E. Lähderanta, M. Mikhailov and I. Kolesnikov, *J. Lumin.*, 2018, **195**, 61–66.
52 N. Stopikowska, M. Runowski, P. Woźny, S. Goderski and S. Lis, *J. Lumin.*, 2020, **228**, 117643.
53 R. Wu, J. Zhou, L. Lei, S. Zhang, Z. Xiao, J. Zhang and S. Xu, *Chem. Phys. Lett.*, 2017, **667**, 206–210.
54 R. S. Melo, J. C. S. Filho, N. S. Camilo, T. I. Rubio, D. Manzani and A. A. Andrade, *Mater. Res. Bull.*, 2023, **157**, 112031.
55 L. Đ. Far, S. R. Lukić-Petrović, V. Đorđević, K. Vuković, E. Glais, B. Viana and M. Dramićanin, *Sens. Actuators, A*, 2018, **270**, 89–96.
56 F. Baumann, T. Paul, S. Wassersleben, R. Regenthal, D. Enke and A. Aigner, *Pharmaceutics*, 2022, **14**, 1184.
57 X. Hong, X. Zhong, G. Du, Y. Hou, Y. Zhang, Z. Zhang, T. Gong, L. Zhang and X. Sun, *Sci. Adv.*, 2020, **6**, eaaz4462.
58 F. Benkő, K. Kristó and T. Sovány, *Pharmaceuticals*, 2025, **18**, 1392.
59 E. Ahmadi, N. Dehghannejad, S. Hashemikia, M. Ghasemnejad and H. Tabebordbar, *Drug Delivery*, 2014, **21**, 164–172.
60 S. Mohanty, M. Lederer, J. García-Balduz, S. Premcheska, A. G. Skirtach, K. Van Hecke and A. M. Kaczmarek, *ACS Omega*, 2025, **10**, 52360–52374.
61 J. M. Unagolla and A. C. Jayasuriya, *Eur. J. Pharm. Sci.*, 2018, **114**, 199–209.
62 M. Licciardi, C. Scialabba, G. Cavallaro, C. Sangregorio, E. Fantechi and G. Giammona, *J. Biomed. Nanotechnol.*, 2013, **9**, 949–964.
63 L. Mahmood, *J. Health Res. Rev.*, 2014, **1**, 5–9.
64 W.-J. Chen and R.-F. S. Huang, *J. Nutr. Biochem.*, 2018, **53**, 28–38.

